

<b>REPORT DOCUMENTATION PAGE</b>				<i>Form Approved OMB No. 0704-0188</i>	
<small>The public reporting burden for this collection of information is estimated to average 1 hour per response, including the time for reviewing instructions, searching existing data sources, gathering and maintaining the data needed, and completing and reviewing the collection of information. Send comments regarding this burden estimate or any other aspect of this collection of information, including suggestions for reducing the burden, to the Department of Defense, Executive Services and Communications Directorate (0704-0188). Respondents should be aware that notwithstanding any other provision of law, no person shall be subject to any penalty for failing to comply with a collection of information if it does not display a currently valid OMB control number.</small>					
<b>PLEASE DO NOT RETURN YOUR FORM TO THE ABOVE ORGANIZATION.</b>					
<b>1. REPORT DATE (DD-MM-YYYY)</b>		<b>2. REPORT TYPE</b>		<b>3. DATES COVERED (From - To)</b>	
<b>4. TITLE AND SUBTITLE</b>				<b>5a. CONTRACT NUMBER</b>	
				<b>5b. GRANT NUMBER</b>	
				<b>5c. PROGRAM ELEMENT NUMBER</b>	
<b>6. AUTHOR(S)</b>				<b>5d. PROJECT NUMBER</b>	
				<b>5e. TASK NUMBER</b>	
				<b>5f. WORK UNIT NUMBER</b>	
<b>7. PERFORMING ORGANIZATION NAME(S) AND ADDRESS(ES)</b>				<b>8. PERFORMING ORGANIZATION REPORT NUMBER</b>	
<b>9. SPONSORING/MONITORING AGENCY NAME(S) AND ADDRESS(ES)</b>				<b>10. SPONSOR/MONITOR'S ACRONYM(S)</b>	
				<b>11. SPONSOR/MONITOR'S REPORT NUMBER(S)</b>	
<b>12. DISTRIBUTION/AVAILABILITY STATEMENT</b>					
<b>13. SUPPLEMENTARY NOTES</b>					
<b>14. ABSTRACT</b>					
<b>15. SUBJECT TERMS</b>					
<b>16. SECURITY CLASSIFICATION OF:</b>			<b>17. LIMITATION OF ABSTRACT</b>	<b>18. NUMBER OF PAGES</b>	<b>19a. NAME OF RESPONSIBLE PERSON</b>
a. REPORT	b. ABSTRACT	c. THIS PAGE			<b>19b. TELEPHONE NUMBER (Include area code)</b>

## PUBLICATION OR PRESENTATION RELEASE REQUEST

Pubkey: 5166

NRLINST 5600.2

1. REFERENCES AND ENCLOSURES	2. TYPE OF PUBLICATION OR PRESENTATION	3. ADMINISTRATIVE INFORMATION
Ref: (a) NRL Instruction 5600.2 (b) NRL Instruction 5510.40D	( ) Abstract only, published ( ) Book ( ) Conference Proceedings (refereed) ( ) Invited speaker (X) Journal article (refereed) ( ) Oral Presentation, published ( ) Other, explain	STRN <u>NRL/JA/7330-06-7030</u> Route Sheet No. <u>7330/</u> Job Order No. <u>73-8404-07-5</u> Classification <u>X</u> U C Sponsor <u>ONR BASE</u> approval obtained <u>yes</u> <u>X</u> no
Encl: (1) Two copies of subject paper (or abstract)	( ) Abstract only, not published ( ) Book chapter ( ) Conference Proceedings (not refereed) ( ) Multimedia report ( ) Journal article (not refereed) ( ) Oral Presentation, not published	

## 4. AUTHOR

Title of Paper or Presentation

Assimilation of HF radar-derived radials and total currents in the Monterey Bay area

Author(s) Name(s) (First, MI, Last), Code, Affiliation if not NRL

Igor G. Shulman, Jeffrey D. Paduan

It is intended to offer this paper to the Deep-Sea Research

(Name of Conference)

(Date, Place and Classification of Conference)

and/or for publication in Deep-Sea Research, Unclassified

(Name and Classification of Publication)

(Name of Publisher)

After presentation or publication, pertinent publication/presentation data will be entered in the publications data base, in accordance with reference (a).

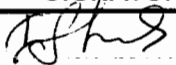
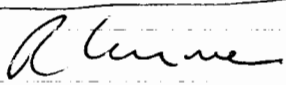
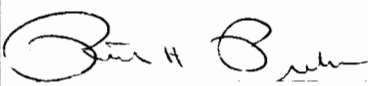

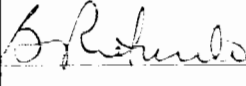
It is the opinion of the author that the subject paper (is       ) (is not X) classified, in accordance with reference (b).This paper does not violate any disclosure of trade secrets or suggestions of outside individuals or concerns which have been communicated to the Laboratory in confidence. This paper (does       ) (does not X) contain any military critical technology.This subject paper (has       ) (has never X) been incorporated in an official NRL Report.

Igor G. Shulman, 7331

Name and Code (Principal Author)

(Signature)

## 5. ROUTING/APPROVAL

CODE	SIGNATURE	DATE	COMMENTS
Author(s) Igor Shulman, 7331		10/20/2006	Need by 10 Nov 06
Section Head <del>J. Kindle, 7331</del>		10/20/2006	Publicly Accessible Sources used for this publication
Branch Head Robert A Arnone, 7330		10/23/06	1. Release of this paper is approved. 2. To the best knowledge of this Division, the subject matter of this paper (has <u>      </u> ) (has never <u>X</u> ) been classified.
Division Head Ruth H. Preller, 7300		11/1/06	1. Paper or abstract was released. 2. A copy is filed in this office. @SSC-4574-L
Security, Code 1226		10/26/2006	
Office of Counsel, Code 1008.3			
ADOR/Director NCST E.O. Hartwig, 7000			
Public Affairs (Unclassified/ Unlimited Only), Code 7030.4			
Division, Code			
Author, Code			

PUBLICATION OR PRESENTATION RELEASE REQUEST **06-1226-3468** Pubkey: 5186

NRLINST 5600.2

1. REFERENCES AND ENCLOSURES		2. TYPE OF PUBLICATION OR PRESENTATION		3. ADMINISTRATIVE INFORMATION	
Ref: (a) NRL Instruction 5600.2 (b) NRL Instruction 5510.40D	( ) Abstract only, published ( ) Book ( ) Conference Proceedings (refereed) ( ) Invited speaker <input checked="" type="checkbox"/> ( ) Journal article (refereed) ( ) Oral Presentation, published ( ) Other, explain	( ) Abstract only, not published ( ) Book chapter ( ) Conference Proceedings (not refereed) ( ) Multimedia report ( ) Journal article (not refereed) ( ) Oral Presentation, not published	STRN <u>NRL/JA/7330-08-7030</u> Route Sheet No. <u>7330</u> Job Order No. <u>73-8404-07-5</u> Classification <u>X</u> U <u>    </u> C <u>    </u> Sponsor <u>ONR BASE</u> approval obtained <u>    </u> yes <u>X</u> no		
Encl: (1) Two copies of subject paper (or abstract)					
<b>AUTHOR</b> Title of Paper or Presentation <u>Assimilation of HF radar-derived radials and total currents in the Monterey Bay area</u> Author(s) Name(s) (First, MI, Last), Code, Affiliation if not NRL <u>Igor G. Shulman, Jeffrey D. Paduan</u> It is intended to offer this paper to the <u>Deep-Sea Research</u> (Name of Conference) (Date, Place and Classification of Conference) and/or for publication in <u>Deep-Sea Research, Unclassified</u> (Name and Classification of Publication) (Name of Publisher) After presentation or publication, pertinent publication/presentation data will be entered in the publications data base, in accordance with reference (a). It is the opinion of the author that the subject paper (is <u>    </u> ) (is not <u>X</u> ) classified, in accordance with reference (b). This paper does not violate any disclosure of trade secrets or suggestions of outside individuals or concerns which have been communicated to the Laboratory in confidence. This paper (does <u>    </u> ) (does not <u>X</u> ) contain any military critical technology. This subject paper (has <u>    </u> ) (has never <u>X</u> ) been incorporated in an official NRL Report. <u>Igor G. Shulman, 7331</u> Name and Code (Principal Author)					
<b>4. SIGNATURE/REVIEW</b>					
CODE	SIGNATURE	DATE	COMMENTS		
Author(s) Igor Shulman, 7331	<i>[Signature]</i>	10/20/2006	Need by 10 Nov 06		
Section Head <u>J. Kindle, 7331</u>	<i>[Signature]</i>		Publicly Accessible Sources used for this publication		
Branch Head Robert A Amone, 7330	<i>[Signature]</i>	10/20/2006			
Division Head Ruth H. Preller, 7300	<i>[Signature]</i>	10/27/06	1. Release of this paper is approved. 2. To the best knowledge of this Division, the subject matter of this paper (has <u>    </u> ) (has never <u>X</u> ) been classified.		
Security, Code 1226	<i>[Signature]</i>	10/27/06	1. Paper or abstract was released. 2. Accepted for release <u>@SSC-464-L</u>		
Office of Counsel, Code 1008.3					
ADOR/Director NCST E.O. Hartwig, 7000					
Public Affairs (Unclassified/ Unlimited Only), Code 7030.4			This is a Final Security Review. Any changes made in the document after approved by Code 1226 nullify the Security Review.		
Division, Code					
Author, Code					

S



# Surface circulation in the Iroise Sea (W. Brittany) from high resolution HF radar mapping

Alexei Sentchev <sup>a,\*</sup>, Philippe Forget <sup>b</sup>, Yves Barbin <sup>b</sup>, Max Yaremchuk <sup>c</sup>

<sup>a</sup> Laboratoire d'Océanologie et Géosciences (CNRS-UMR8187), Université du Littoral - Côte d'Opale, 62930 Wimereux, France

<sup>b</sup> Laboratoire de Sondages Electromagnetiques de l'Environnement Terrestre (CNRS-UMR6017), Université du Sud Toulon Var, 83130 La Garde, France

<sup>c</sup> Naval Research Laboratory, Bldg. 1009, Stennis Space Center, MS 39529, USA

## ARTICLE INFO

### Article history:

Received 10 September 2010

Received in revised form 9 November 2011

Accepted 29 November 2011

Available online 11 December 2011

### Keywords:

HF radar

Tidal current

Residual flow

Eddy field

Iroise Sea

## ABSTRACT

The data from two high-frequency radars (HFR) operating in the Iroise Sea are re-processed by applying an improved version of the direction finding algorithm, removing wave-induced surface currents and the variational interpolation on a regular grid. Combining these processing techniques allowed reconstruction of the surface currents at a level of details that was not previously available. Refined resolution enabled to identify fine-scale structures of surface circulation, to quantify the variability of tidal currents and the residual (time averaged) velocity field, and to explain spatial intermittence in polarization of the tidal current ellipses. The analyzed data span two month-long periods in spring and late summer of 2007. The major findings include (a) a dipole structure in the vorticity field characterized by two oppositely rotating eddies, generated on the leeward side of the Ushant Island at flood (negative polarity) and at ebb (positive polarity); (b) an extremely strong fortnightly variability of tidal currents northwest of the Ushant Island with the highest velocity magnitude of 3.9 m/s caused by the interference of the major semi-diurnal tidal constituents; (c) a significant contribution of the higher order nonlinear tidal harmonics to the surface currents in the Fromveur strait, which maintains strong tidal currents and affects the shape of their fortnightly modulation. The residual circulation is characterized by two distinct zones approximately separated by the 100 m isobath: in the offshore zone the residual currents have a significant contribution of the wind-driven component, whereas the nearshore zone is characterized by extremely strong (up to 0.4 m/s) time-independent residual circulation featuring two permanent anticyclonic eddies: north of the western extremity of the Sein archipelago, and north the Ushant Island. The acquired data and the presented results could be useful for regional model validation and studies of the local eddy dynamics, tidal fronts, and passive tracer transport in the region.

© 2011 Elsevier B.V. All rights reserved.

## 1. Introduction

In recent years, high-frequency (HF) Doppler radar systems have had stunning success in the mapping of surface currents. The ability to map surface circulation in coastal ocean areas has brought new insights to the complexities of physical processes in nearshore waters, and allowed significant advances in our understanding of circulation and oceanographic conditions in many coastal regions (e.g. Bassin et al., 2005; Breivik and Sætra, 2001; Haus et al., 2000; Kaplan et al., 2005; Kovacevic et al., 2004; Marmorino et al., 1999; Sentchev et al., 2009a, 2009b; Yoshikawa et al., 2007).

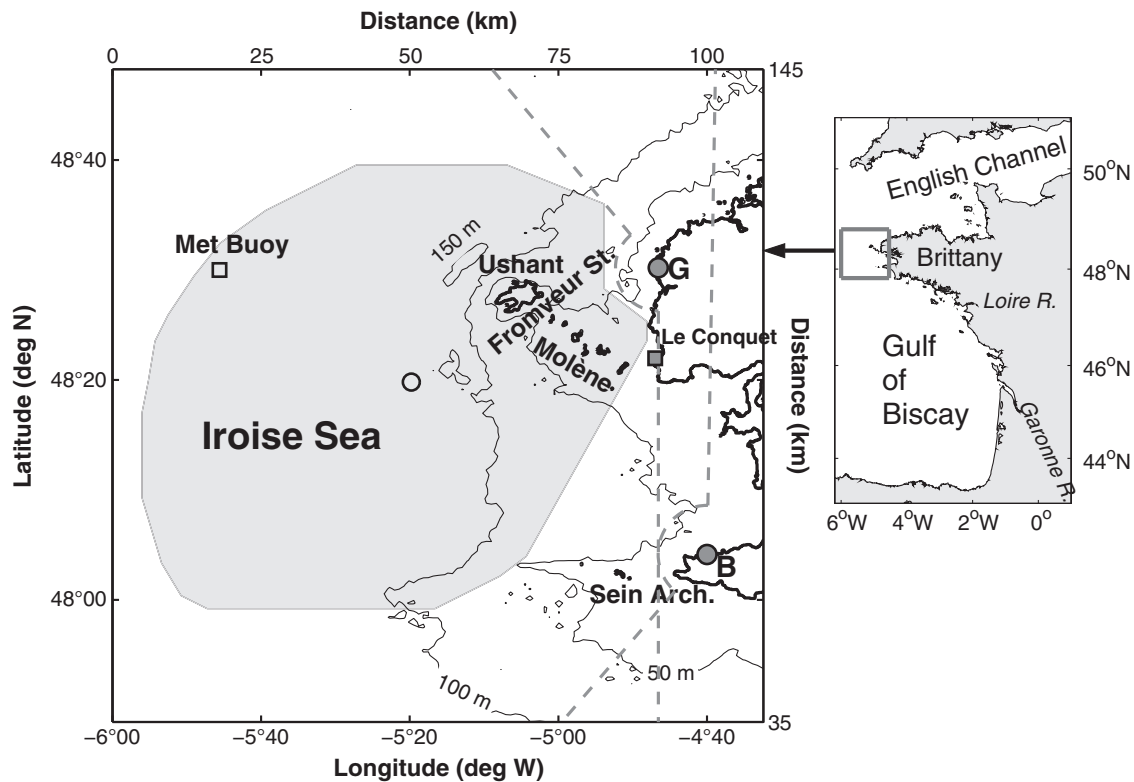
Iroise Sea is one of the regions, continuously monitored by HF radars since 2006 (Fig. 1). A system, composed of two high-frequency Wellen Radars (WERA) operating at 12.4 MHz, is deployed on the

western Brittany coast to monitor surface currents up to 140 km offshore. The Iroise Sea circulation is very difficult to study by *in situ* methods, as it is dominated by extremely strong tidal currents, often exceeding 3 m/s, and affected by strong and often violent westerly and southwesterly winds. Low pressure atmospheric systems (cyclones), generated in the Northwestern Atlantic, regularly cross the Iroise Sea and might cause significant surges on the West Brittany coast with sea surface rise up to 0.50 m (Bouligand and Pirazzoli, 1999). Surface currents in the Iroise Sea are also affected by swell and wind waves. Violent storms, often occurring in winter, contribute to the reputation of the Iroise Sea as one of the most dangerous seas in Europe.

Circulation in the Iroise Sea has been studied previously by many authors by means of field measurements (Le Boyer et al., 2009; Mariette and Le Cann, 1985; Pingree et al., 1975) and numerical modelling (Mariette et al., 1982; Muller et al., 2009, 2010). These studies investigated the character of local geostrophic and tidal circulations, eddy frontal dynamics and shed light on the role of tidal mixing in controlling cross-frontal heat and mass exchange. They also

\* Corresponding author.

E-mail addresses: [alexei.sentchev@univ-littoral.fr](mailto:alexei.sentchev@univ-littoral.fr) (A. Sentchev), [philippe.forget@lseet.univ-tln.fr](mailto:philippe.forget@lseet.univ-tln.fr) (P. Forget), [yves.barbin@lseet.univ-tln.fr](mailto:yves.barbin@lseet.univ-tln.fr) (Y. Barbin), [max.yaremchuk@nrlssc.navy.mil](mailto:max.yaremchuk@nrlssc.navy.mil) (M. Yaremchuk).



**Fig. 1.** Location of the Iroise Sea and HFR survey area (grey square contour on the right panel). Experimental domain in the Iroise Sea (grey shading) and radar coverage zone (left panel). Radar sites are shown by grey circles. Grey broken contours show coverage area for individual radars. Squares denote locations of the met buoy and tidal gauge station. Open circle indicates the location of the grid point where wave induced component of surface current was analyzed in detail (cf. Fig. 2 d and Fig. 3b). Contour interval of the bathymetry is 50 m (grey solid lines). Grey dashed lines show coverage areas for the individual radars. Geographic names used in the text are also shown.

allowed better understanding of the role that different physical forcing mechanisms play in the Lagrangian circulation of the basin. In particular, the influence of the bottom thermal front on surface circulation and large-scale eddy motions associated with frontal dynamics were evidenced in (Le Boyer et al., 2009; Muller et al., 2009). However, with the exception of the recent field study of Le Boyer et al. (2009), it is difficult to find a detailed observation-based description of the circulation in this area in literature. Quantitative estimates of the small scale circulation features, their magnitude and dependence on various forcing factors remain relatively uncertain. This shortcoming is primarily due to the difficulties in acquisition of the long-term high-resolution *in situ* data because of the extremely strong currents and severe meteorological conditions in this part of the Atlantic Ocean. Complexity of the physical processes occurring in the Iroise Sea in conjunction with complex topography renders modelling of the circulation also difficult. In that respect, remote sensing of surface currents by HF radars (HFR) provides a unique opportunity to establish a monitoring system in the basin on a regular basis.

As the experimental data required for model validation have been extremely scanty until recently, in 2005, the French Naval Oceanographic Centre (SHOM) put forward an initiative to perform the HFR observations of surface circulation in the Iroise Sea. The experiment was designed to get better knowledge on physical processes governing the circulation and to perform the validation of numerical models. Beam Forming (BF) algorithm actually used for processing the radar data in nearly real-time (Mariette et al., 2006) provides radial velocities of surface current along sixteen beams with 9° azimuthal discretization. The angular resolution of the system is too coarse and, to our opinion, unable to capture the fine scale structure of the surface flow, especially around the islands and in the Fromveur Strait which are of particular interest.

In the present study we address two challenges.

First, we perform high resolution surface current mapping in both temporal and spatial dimensions (20 min and 1 km) by applying a novel approach to the raw HFR data processing in conjunction with high-performance variational interpolation technique. High azimuthal resolution of the radial velocities is achieved by the HFR signal processing using an improved version of the MUSIC direction finding algorithm (Lipa et al., 2006). The radial velocities are then interpolated on the regular grid using a variational 2dVar method (Yaremchuk and Sentchev, 2009, referred hereafter as YS09). Furthermore, the contribution of surface waves to the radar derived velocities is estimated with the method recently developed by Arduin et al. (2009). These three techniques have been implemented for processing of HFR data for two selected periods: in spring and late summer 2007 representing in total 52 days. The summer period is synchronized with the extensive field experiment in the Iroise Sea abroad of the R/V “Côtes de la Manche” (Le Boyer et al., 2009).

Second, we study the resulting surface circulation patterns from the perspective of different modes of variability. We focus on physical processes governing the tidal currents and residual circulation in the area. The HFR observations revealed flow complexity and variability at a level of details that were not previously available. Refined resolution allowed us to identify fine-scale structures of surface circulation, to quantify the variability of tidal currents and residual velocity field, and to explain patchiness in polarization of tidal current ellipses.

The paper is organized as follows. In Section 2, we present the study site, the environmental data (recorded and derived from numerical modeling) during selected periods of the radar experiment, the HFR network, and briefly describe the methods of analysis. In Section 3, we describe and analyze the observed features of surface circulation, flow variability, and the fine-scale structures in vorticity and residual velocity fields in the Iroise Sea. Discussion of the results and summary are presented in Section 4.

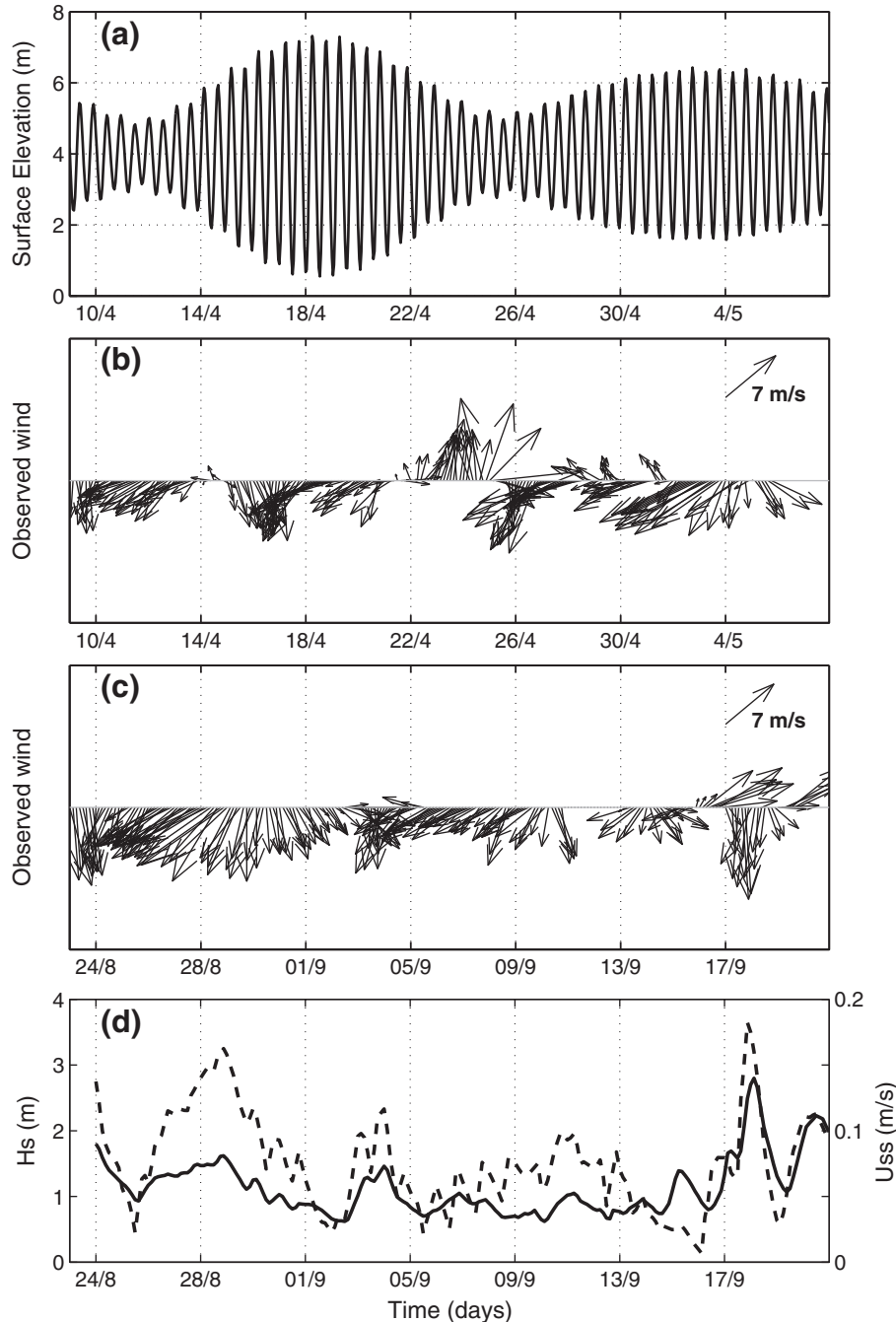
## 2. Data and methods

### 2.1. Study site and environmental conditions

The study site, Iroise Sea, is located in the extreme north-eastern part of the Gulf of Biscay (Fig. 1). This is a shallow water area with depth gradually decreasing westward from 50 to 150 m with more gentle bottom slope in the South. In the North, there is a group of small islands, islets and rocks that form Molène archipelago, and a bigger,  $8 \times 4$  km, Ushant Island. It is separated from the Molène Islands by the 2 km wide and 50 m deep Fromveur strait. In the

southern part, there is a group of islets and rocks belonging to the Sein archipelago. Only a part of it is exposed at low tide.

In the Iroise Sea, tidal currents are generally characterized by clockwise rotation in response to the joint effect of the Coriolis force and sea surface gradients related to tidal wave propagation. Incident tidal waves arrive from the Gulf of Biscay, travel around the W. Brittany Peninsula and enter the English Channel. The tidal waves' interactions is the dominant factor that determines variability of the sea surface height (SSH) and currents in the region. The SSH variability in the Le Conquet harbor exposes variations of 2 to 7 m (Fig. 2a), with the predominant semi-diurnal period, small diurnal inequality



**Fig. 2.** External forcing data. (a) Tidal elevation observed in Le Conquet harbour in April–May 2007. Wind measurements made at Met Buoy within the radar coverage zone during April–May (b) and August–September 2007 (c) (Regional Met-office data). Arrows show observed wind direction. Wind speed scale is given in the right upper corner. (d) 3-h data of significant wave height,  $H_s$  (solid line), and wave-induced velocity,  $U_{ss}$  (dashed line), in August–September 2007 in the middle of the study area. See Fig. 1 for location of measurement points.



and pronounced fortnightly modulation due to the interference of the semi-diurnal ( $M_2$ ,  $S_2$ ,  $N_2$ ) and quarter-diurnal ( $M_4$ ,  $MS_4$ ) constituents. Both primary and secondary spring tides occur during the period shown. Tidal velocities and transports show fortnightly variability in response to the spring-neap cycle.

Buoyancy forcing in the domain is relatively weak. The majority of freshwater comes from the Aulne and smaller rivers located on the western Brittany coast. Their discharge to the Iroise Sea of approximately  $60 \text{ m}^3/\text{s}$  observed in April 2007 (<http://www.hydro.eaufrance.fr>) can be considered as negligible, compared to discharge of the Loire and Garonne rivers into the central part of the Gulf of Biscay ( $1200$  and  $900 \text{ m}^3/\text{s}$  respectively) during the same period. Great distance between these rivers' mouths and the Iroise Sea favors the fresh water dispersion and only a small quantity of freshwater reaches the western Brittany coast.

Fig. 2b shows winds measured at the offshore met buoy (see Fig. 1 for buoy location). Two distinct wind regimes were observed during the spring period. Between the 10th and 22th of April, (the first 12-day period), winds were generally coming from the North and North-East with moderate speeds ranging from  $5$  to  $8 \text{ m/s}$ . From April 22 until May 5, variable wind regime was observed with small domination of northeasterly winds with speeds up to  $10 \text{ m/s}$ . During the late summer period, the winds, generally stronger, were blowing mostly from the northern and north-eastern sectors (Fig. 2c).

The spectrum of the hourly winds recorded by the offshore Met buoy is given in Fig. 3a. Spectral analysis of both zonal and meridional wind components and the total kinetic energy of the wind shows the red nature of the spectrum which follows a power law with spectral slope close to  $-5/3$ , mainly in higher frequency band ( $>1 \text{ cyc/d}$ ). The spectrum reveals a variety of atmospheric motions with significant peaks at diurnal and sub-diurnal frequencies ( $0.55$ ,  $0.35$ , and  $0.2 \text{ cyc/d}$ ). Diurnal peak evidences the effect of sea breeze, whereas other significant peaks are within the range of cyclonic-anticyclonic frequencies. They are certainly related with cyclonic activity over the North Atlantic. Small scale variability of the local winds has

been documented by Muller et al. (2007) who found a slight systematic variation of the wind direction in the area between the Ushant Island and the Brittany coast.

## 2.2. HFR data and methods of processing

### 2.2.1. HFR velocity data

A system of two high-frequency Wellen Radars (WERA) operating at  $12.4 \text{ MHz}$  is deployed on the western Brittany coast from July 2006 to date. Individual radar sites are located at Cape Garchine (site G), a seashore flat-ground area, and Cape Brezellec (site B),  $50 \text{ km}$  southward. At both sites, transmission is done by an endfire array of four antennas forming a rectangle. The receiving array contains 16 equally spaced antennas parallel to the shore line and stretched along  $150 \text{ m}$ .

The Beam forming (BF) method, actually used for processing the radar data in near real-time, provides radial velocities of surface current along beams with  $3 \text{ dB}$  width of  $9^\circ$  on the average. An automatic RFI (Radio Frequency Interference) clearing has been integrated into signal processing algorithm (Gurgel and Barbin, 2008), along with the quality control for removing outliers and radial velocities exceeding  $4 \text{ m/s}$ . The radial (along beam) resolution is  $1.5 \text{ km}$  and the range is of the order of  $140 \text{ km}$ . In practice, for optimal implementation of the RFI clearing method, the data were processed up to a range of  $120 \text{ km}$ .

Radial velocities from two radars are combined to provide surface current maps at 20-min acquisition rate ([http://www.previmer.org/observations/courants/radar\\_hf\\_iroise](http://www.previmer.org/observations/courants/radar_hf_iroise)). The accuracy of the radar-derived velocities has been estimated by SHOM (Oceanographic Division of the French Navy) through a comparison with surface drifters and ADCP current measurements for a period of 7 months. In the majority of situations, the discrepancy in velocity measured by different instruments did not exceed  $0.15 \text{ m/s}$  (Le Boyer et al., 2009). It was also noticed that a large fraction of this discrepancy might not be due to instrumental errors, but to the definition of the “surface

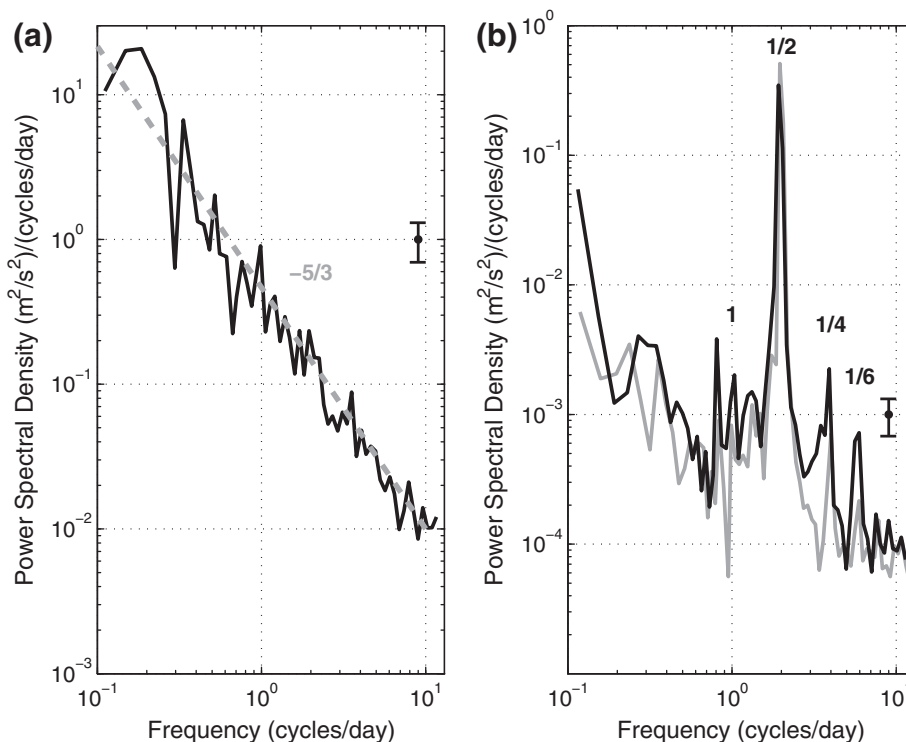


Fig. 3. Power spectra of the wind and HF radar data. (a) Wind spectrum recorded at the Met buoy in April–May 2007. (b) Kinetic energy spectra at the same period for two selected grid points of the radar coverage zone: a point closest to the Met buoy (black line) and a point in the central part of the zone (grey line). See Fig. 1 for point location. Numbers stand for dominant tidal period (in days). Error bar indicates 95% confidence interval.

velocity”, as other measurement techniques are sensitive to the shear of the Eulerian current, to Stokes drift, to the sea state, etc.

Despite a good quality of the radial velocities recorded by the radars, angular resolution of the system is relatively coarse and does not capture the fine scale structure of the surface flow, especially around Ushant-Molène Islands and in the Fromveur strait which are of particular interest.

### 2.2.2. Application of the direction finding method for processing the radar data

To obtain higher resolution radial velocity maps, the HFR signals were reprocessed by using the Multiple Signal Classification (MUSIC) direction finding (DF) algorithm of Schmidt (1986) driven by the parameterization of Lipa et al. (2006). In contrast to BF, the DF method seeks for the bearings from which the energetic Doppler lines originate. If no solution is delivered in a given direction slot, then the DF method leaves a gap in the velocity record. If multiple Doppler shift solutions are delivered in the same bin, a power averaged Doppler shift value is calculated. The maximum value of radial velocity measured by a radar operating at a wavelength  $\lambda$  (12.4 MHz) is limited by  $f_B \cdot \lambda/2$  (4.3 m/s), where  $f_B$  is the Bragg frequency (0.359 Hz) corresponding to the radar frequency.

Processed directions spanned the aperture from  $-70^\circ$  to  $70^\circ$  with respect to the normal line of the receiving antenna array, thus providing the azimuthal resolution of  $2^\circ$ . The azimuthal resolution varies along a given beam from 0.35 km (1.6 km for BF) to 2.8 km (12.6 km for BF) at 10 and 80 km range, respectively.

Fig. 4 shows radial velocities provided by BF and DF methods for the same acquisition time. In general, similar spatial patterns on both velocity maps are found. However the pattern on the BF map is smeared in azimuth and it can be difficult to determine the spatial extension or the limits for different structures in the velocity field. Detailed analysis of velocity maps for different periods of tidal cycle revealed that the magnitude and spatial variation of the velocity field were poorly represented by BF algorithm. However, the enhanced resolution provided by the DF method inherently introduces gaps (see above) and noise in the radial velocity field (Fig. 4b). Noise comes from the fact that the velocity estimated at a given range for a particular bearing can originate from another bearing depending on the complexity of the ocean wave and current conditions (Barrick and Lipa, 1996, 1997). The variational method used for radial velocity interpolation from both radar units (Section 2.2.3) performs gap filling and offers an efficient control of the noise level.

The DF technique was applied to the HFR data to retrieve radial velocities for two selected periods, namely, from 10 April to 5 May, and from 24 August to 19 September 2007. The second period was of particular interest because it coincided with extensive field experiment (Le Boyer et al., 2009). During these periods, both radars worked continuously with low data loss. Fractional availability of radial velocity data for both radars during the two periods is shown in Fig. 5. The data were available in at least 50% of time within a cone with a radius of approximately 100 km. Despite of its low altitude (20 m), the Ushant Island strongly affects availability of radar data providing drops in the data return to 25% (for site B) and to 50% (for site G) behind the island. The fractions of the data return by the individual radars are shown in Fig. 5 by thin contours. The interpolation grid given by the bold contour has approximately 4000 points, equally spaced by 1.1 km, and covers a nearly circular area with the seaward limit of 90 km from the coast. The condition of 50% availability of the radial velocity data is met in the majority of the interpolation area with the exception of the northern part for site B. The angle between radar beams at points of beam intersection was greater than  $30^\circ$  all over the interpolation area.

### 2.2.3. Variational interpolation

Velocity vector maps were generated from radial velocity data using the variational interpolation technique, 2dVar (YS09). This is non-local, kinematically constrained algorithm. It uses a combination of radial velocities at all measurement points to reconstruct the velocity vector in one location. This feature of the interpolating technique can help to overcome some limitations related to a lack of data. The smoothness of the interpolated vector field is enforced by penalizing the squared Laplacian of velocity and also of its curl and divergence, thus providing the algorithm with flexibility and efficient control of smoothness. Kinematic constraints (zero flux on rigid boundary), incorporated into 2dVar, appear particularly useful given a large number of islands in the study area. The 2dVar interpolation was developed and employed to reconstruct vector current fields using synthetic data with different (up to 50%) signal/noise ratios and also a real data set from the radar experiment in Bodega Bay, northern California, in the Gulf of Lion, western Mediterranean (Sentchev et al., 2009a, 2009b), and demonstrated certain advantages compared to alternative interpolation techniques (e.g., local interpolation, OMA (Muller et al., 2009)).

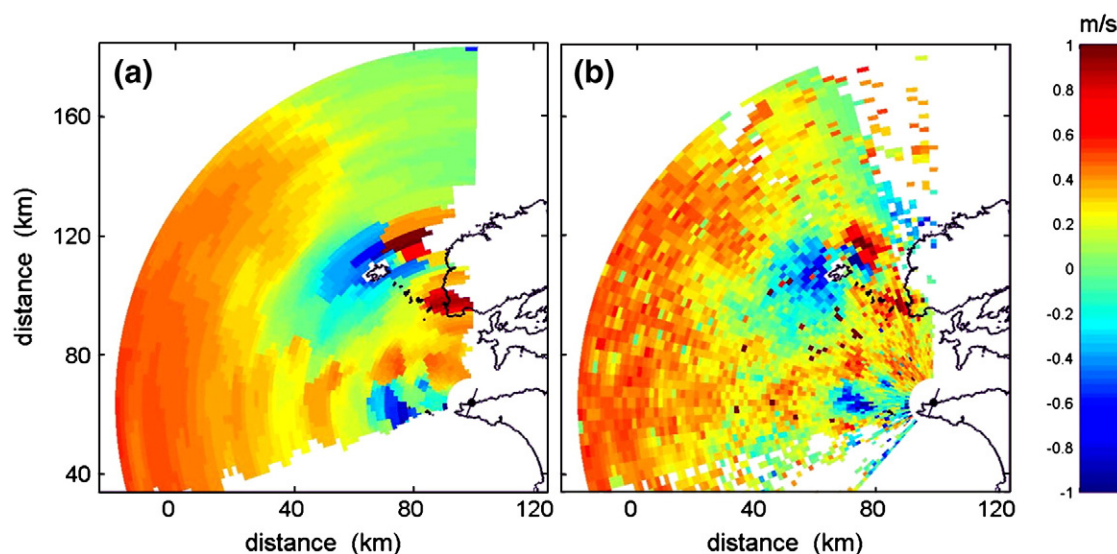


Fig. 4. Radial velocity maps on April 17, 2007 (4:10 am) derived from radar data processing by (a) beam forming and (b) direction finding methods.



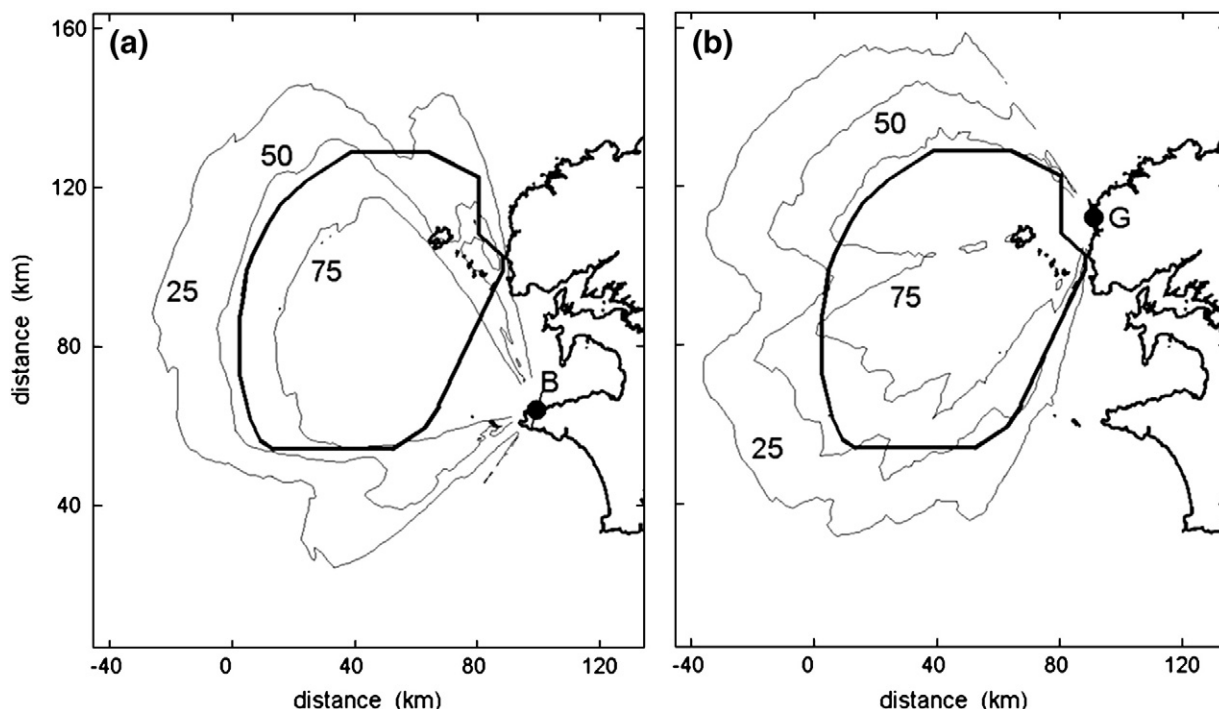


Fig. 5. Cumulative availability of the radial velocity data (in per cent) for radar station B (a) and G (b) during the two periods of analysis (thin contour lines). Bold contour envelopes the area where surface velocity vectors were generated at each time interval by the variational algorithm.

#### 2.2.4. Velocity errors estimation

The variational approach used for velocity interpolation allows estimating errors of the velocity field (YS09). The inverse error covariance matrix  $C^{-1}$  for gridded velocity is the matrix  $H$  of second derivatives of the cost function with respect to  $u$  and  $v$  (the Hessian matrix of the variational problem). As the matrix  $H$  may not necessarily have the full rank, we seek for its generalized inverse by discarding eigenvectors corresponding to small eigenvalues. Typically, 0.02% of the eigenvectors are rejected during the inversion of  $H$ .

Fig. 6 shows, as an example, the map of errors of interpolated velocity (current vector magnitude) for the first HFR snap shot (00:10

on April 10, 2007). The map combines information about the availability of the data, accuracy of radial velocity measurements, and geometric dilution of precision (GDOP). The resultant velocity errors are less than 15 cm/s in the majority of the domain, and rapidly increase (up to 40 cm/s) in areas poorly covered by observations. The condition on angle intersection ( $<30^\circ$ ), adopted for configuration of the interpolation domain, prevents error growth at far ranges. It should be emphasized that the error distribution corresponding to velocities of the observed circulation pattern does not give the observational signal to noise ratio. This ratio can be derived by comparing the radial velocity maps with spatial distribution of the accuracy of the radial velocity measurements. The latter depends upon the system configuration, level of backscattered energy, sea surface state, variability of currents within the radar measurement cell, ..., and might attain 8–10 cm/s.

#### 2.2.5. Removing the sea state influence

Surface velocity derived from radar data is estimated from the difference between the position of the observed and theoretical Bragg lines on the Doppler spectrum of the sea surface echo (Stewart and Joy, 1974). It is generally assumed that Bragg waves, i.e. waves whose wavelength (at grazing angle) is equal to the half of the electromagnetic wavelength, satisfy the linear dispersion relationship of ocean waves. Considering nonlinearities of the ocean surface, Weber and Barrick (1977) slightly modified this relationship accounting for all types of the surface gravity waves. Broche et al. (1983) provided a theoretical expression which quantifies the effect and can be used to extract the wave induced current component from current radio measurements. The method of velocity correction was recently applied to radar measurements in the Iroise Sea, with a particular interest of studying the wind-current relationship (Ardhuin et al., 2009) locally. In the present paper we apply the method to the whole area of radar coverage. Information on surface waves was provided every 3 h by the numerical wave model WAVEWATCH III at 1/30° resolution (2.5 km) using the implementation described in Ardhuin et al. (2009). Appendix A contains the description of the method applied for estimation of the wave induced surface current velocity vector,

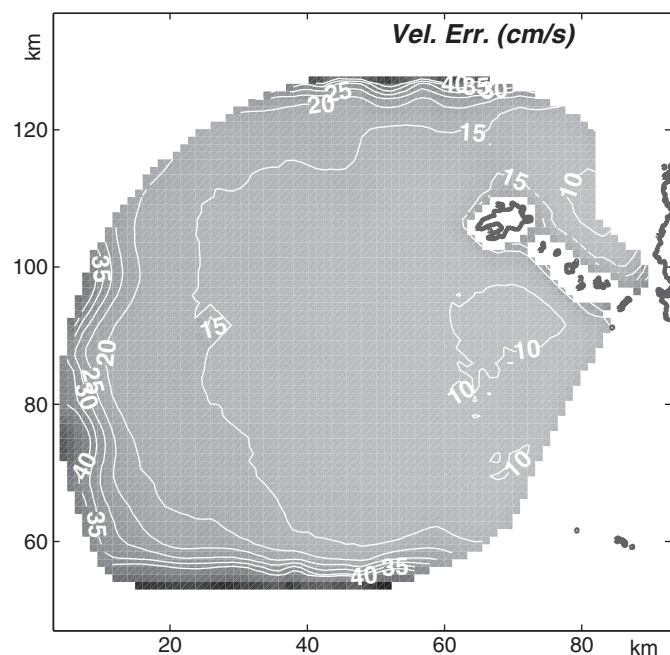


Fig. 6. Velocity errors (cm/s) for a surface current vector map on April 10, 2007, 00:10.

$U_{ss}$ , at the grid points of the wave model. Resulting values of  $U_{ss}$  were spatially interpolated on the regular radar grid, then interpolated in time, and finally subtracted from the radar derived current velocities. For convenience,  $U_{ss}$  will be referred hereafter as Stokes velocity although in practice it represents approximately 85% of the model-estimated Stokes drift velocity (cf. Appendix).

Fig. 2 d provides estimated Stokes velocity and significant wave height during the second (late summer) period of analysis in a point located in the middle of the study area (Fig. 1). Strong correlation is observed between the wind speed and  $U_{ss}$ . Northern winds with high speed, observed on August 29, September 3 and 18 (Fig. 2c), produce surface currents with magnitudes greater than 0.10 m/s. Winds from North–East sector tend to weaken surface waves ( $H_s < 1$  m) and the associated wave induced currents to less than 0.10 m/s (Fig. 2 d).

Fig. 7 summarizes the contribution of Stokes velocity to the surface currents in terms of the occurrence probability of a measured current magnitude  $U$  and the wave induced current velocity  $U_{ss}$ . These statistical estimates cover both studied periods. The modulus of  $U_{ss}$  is a small quantity compared to  $U$  with a peak of occurrence at 0.05 m/s whereas the occurrence peak for  $U$  is 0.40 m/s. The highest magnitude of Stokes current did not exceed 0.18 m/s during the period of interest. Moreover,  $U_{ss}$  values are rather small compared to the precision of radar surface currents. For a point located in the middle of the study area (Fig. 1), the absolute values of the west–east (south–north) components of  $U_{ss}$  exceed the intrinsic error of the corresponding current components, estimated as 4 cm/s (7 cm/s) in 53% (7%) of cases. However the west–east component of  $U_{ss}$  is generally higher than this error and can exceed it 4 times. In that case, removing the sea state influence is useful to improve the quality of current velocity estimates.

### 2.2.6. Principal component and rotary spectral analysis

In order to identify processes governing surface circulation in the Iroise Sea, spectral analysis of velocity records in different locations has been performed. Fig. 3b shows spectral distribution of the total kinetic energy for two selected grid points: a point closest to the Met bouy and a point in the central part of the radar coverage zone (see Fig. 1 for locations). The distribution clearly shows that surface dynamics in the Iroise Sea is dominated by tides. The spectra in Fig. 3b indicate that most of the kinetic energy is distributed between the dominant tidal frequencies: semi-diurnal, quarter-diurnal, sixth-diurnal and diurnal, with prevailing semi-diurnal tide. In sub-tidal

frequency range, there is a moderate rise of energy which reveals motions with 3.3-day period (Fig. 3b). Analysis of similar distribution for the wind (Fig. 3a) does not show any significant atmospheric forcing in tidal band, suggesting the absence of modulation of tidal currents by wind.

Furthermore, we applied the principal component analysis (PCA) technique to this data set in order to quantify tidal flow dynamics. Our approach has a certain advantage over a frequently used harmonic analysis because it allows quantifying the total contribution of all tidal constituents to observed currents and assessing time-space variability of the currents. As tidal currents in the Iroise Sea are rotational, the current velocity vector evolving over a tidal cycle draws an ellipse. Parameters of synthesized ellipses, retrieved from the PCA, provide orientation and magnitude of the dominant current. The anisotropy of oscillatory tidal flow (ellipse eccentricity) is quantified by estimating the eigenvalue ratio of the velocity correlation tensor. The PCA technique does not give, however, information on the sign of rotation of velocity vectors. To fill this gap, we performed rotary spectral analysis (Emery and Thompson, 1997) of velocity time series, referred hereafter as RSA. The technique involves the decomposition of the velocity vector into the clockwise (cw) and counter-clockwise (ccw) rotating circular complex-valued components. First, the RSA was performed to identify the dominant frequency in current velocity variation. Both cw  $S_-$  (negative) and ccw  $S_+$  (positive) power spectra revealed pronounced peaks at the semi-diurnal frequency. After that, the rotary coefficient,  $r = (S_+ - S_-)/(S_+ + S_-)$ , was estimated at every grid point at these peak values.  $r$  ranges from  $-1$  for clockwise motion to  $+1$  for counter-clockwise motion ( $r = 0$  is oscillating non-rotational flow).

We have also estimated the Eulerian residual currents and investigated their relationship with wind forcing.

## 3. Results

### 3.1. Tidal currents: spatial patterns and variability

Spatial and temporal variability of tidal currents is quantified using the parameters of synthesized tidal current ellipses derived from the PCA and RSA. The results are summarized in Fig. 8 for the primary spring tide period. Tidal current ellipses (Fig. 8a) represent the 7-day averaged circulation pattern associated with the tidal wave arriving from the Gulf of Biscay and traveling northeastward toward the English Channel. The detailed analysis of ellipse orientation shows that tidal currents are controlled by the bottom topography and peculiarities of the coastline. These factors tend to align the major axes along the depth contours.

One can distinguish anisotropy of the current field with relatively high ellipse eccentricity in the western part of the region and in two locations in the eastern part: south of the Ushant Is. and in a shallow water region between the Molène Islands and Brittany coast. The former might be related to the current squash against the island producing more circular shape of ellipses. The latter reflects the effect of bottom friction on tidal currents (Defant, 1961).

The spatial distribution of the rotary coefficient (Fig. 8b) shows that currents are rotating clockwise (cw) in the majority of the domain. This feature is related to the spatial pattern of the sea surface gradients which tend to follow the propagation of the tidal wave from the Gulf of Biscay in a broad cw turn around the Brittany Peninsula (e.g. Lux et al., 2010). The Coriolis force acting on the currents reinforces their cw rotation (Defant, 1961).

The maximum negative values of  $r$  (up to  $-0.9$ ) are found in the northeastern part of the region (Fig. 8b). Large positive values (up to 0.7) are observed in three locations around the Ushant and Molène Islands (Fig. 8b), and in the vicinity of the Sein archipelago (not shown). In the shallow water areas, east of Molène and north of Sein islands, the bottom friction comes into play, alternating the

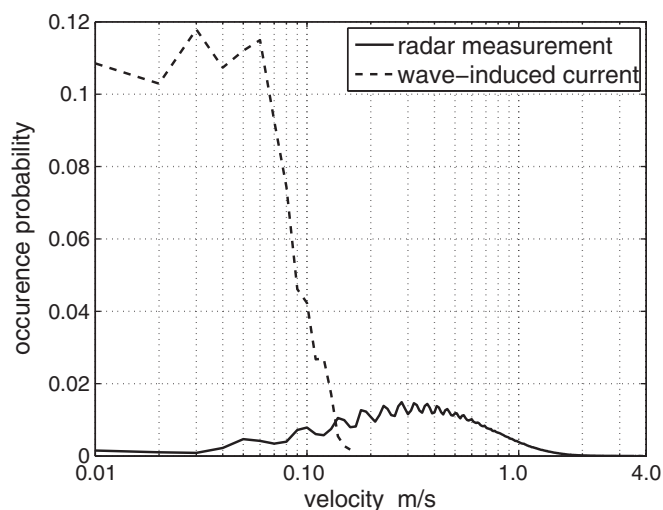
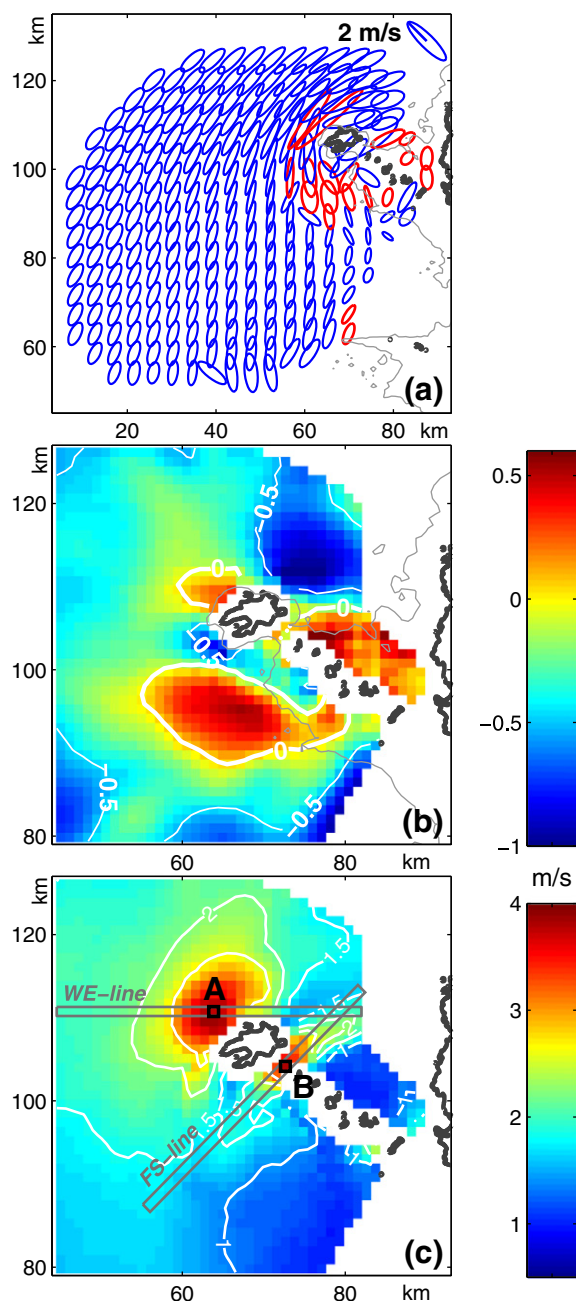


Fig. 7. Probability of occurrence of the velocity magnitude of surface currents derived from radar measurements and the velocity magnitude of wave induced currents (Stokes current).



**Fig. 8.** (a) Tidal current ellipses during spring tide in April 2007 (7-day averaged from 15 to 22 April 2007). Every forth ellipse is shown. Red ellipses denote counter-clockwise rotating currents, blue ones-clockwise rotating currents. Rotary coefficient  $r$  for the same period (b), and amplitude of spring tidal currents (c) in the vicinity of Ushant and Molène Islands. 50 m isobath is shown by thin grey contour. Grey lines in (c) show cross-sections used for analysis of the variability of tidal currents.

sign of current vector rotation, and providing positive polarization of current ellipses.

The largest region of the ccw rotating currents is located south of Ushant and Molène Islands. Positive polarization cannot be caused directly by the bottom friction as the depth exceeds 50 m there. One of the possible mechanisms is the interaction of tidal flow with the Ushant Is. resulting in vorticity production. Positive vorticity, generated by frictional effects on leeward side of the island during the southward ebb tidal flow, is advected westward along the southern periphery of the Ushant and Molène Islands during transition from ebb to flood. This provides an extended region with ccw rotating ellipses there (Fig. 8a). The origin of the negative values of  $r$  observed north of the Ushant Is. (Fig. 8b) can be explained in a similar way. This

patchiness in rotary coefficient distribution with change in sign of rotation of the velocity vectors around the islands is the most notable feature of tidal circulation in the Iroise Sea (Fig. 8a,b).

The magnitude of tidal currents shows significant variations in space and time. During spring tide, current velocity varies from 0.7 to 3.9 m/s (Fig. 8c), during neap tide – from 0.2 to 1.7 m/s (results not shown).

Tidal waves arriving from the Gulf of Biscay propagate in the N-NE direction over steep bottom in the southern part of the Iroise Sea, and spring tide velocities do not exceed 1.5 m/s there. Higher bathymetry gradients in the NE part of the Sea and the presence of islands cause flow acceleration, tend to tighten the streamlines and provide the maximum velocities at the seaward extremity of the Ushant Is. (up to 3.9 m/s) and in the Fromveur Strait (up to 3.8 m/s). We performed detailed analysis of surface current variability in these two locations.

Figs. 9a and 10a show time evolution of the magnitude of tidal currents (semi-major axis of synthesized current ellipses) along two lines crossing the region with strongest currents. The first line, oriented in the west-east direction (WE-line) is located north of Ushant Is. The second passes through the Fromveur Strait (FS-line) and has an oblique orientation (Fig. 8c).

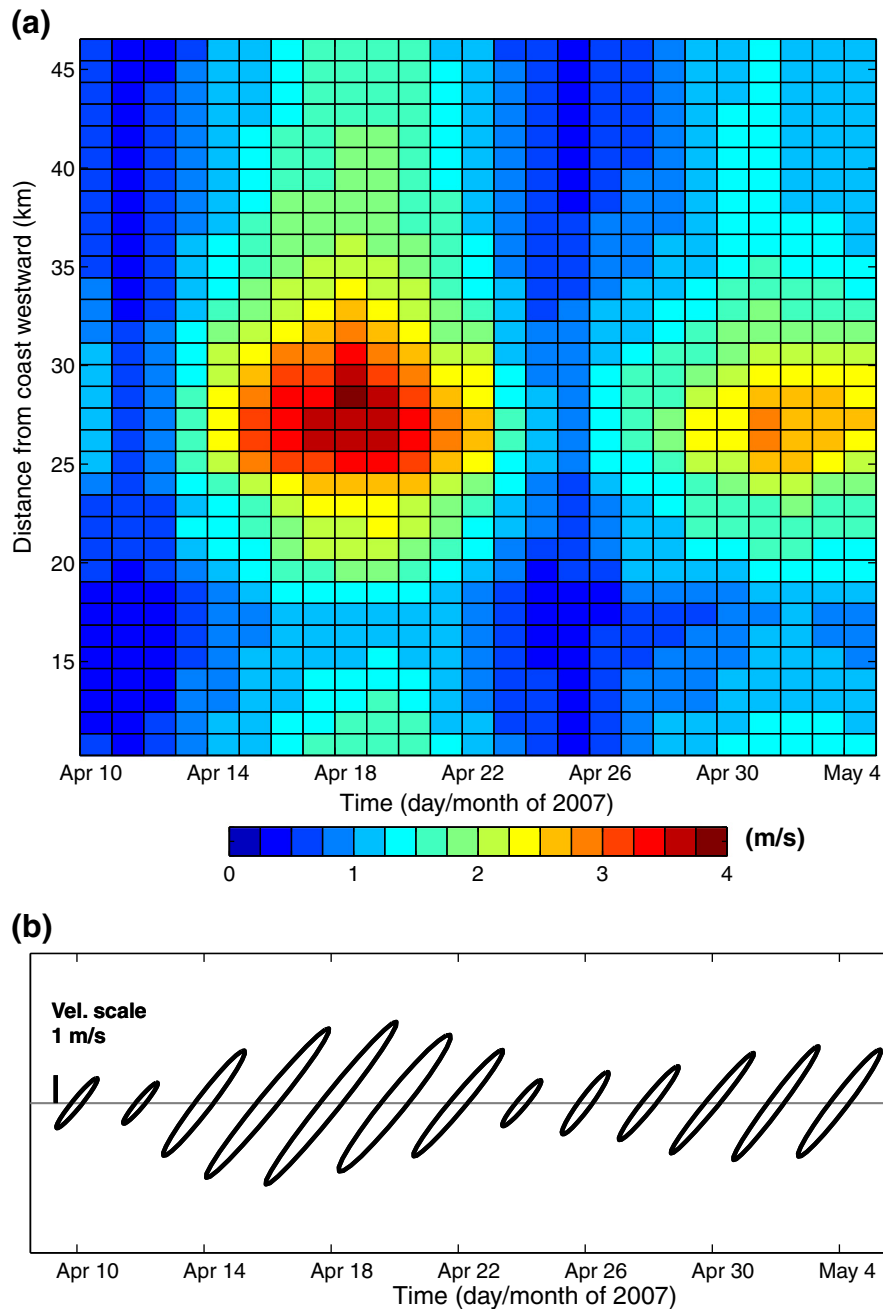
Both primary and secondary spring tides can be recognized in the velocity field. In the central part of the WE-line, at point A located NW of Ushant Is. (Fig. 8c), the magnitude of tidal currents increases more than four times in 8 days, rising from less than 1 m/s on 11 April to 3.9 m/s on 18 April (Fig. 9b). The range of current variability decreases progressively westward and eastward from the maximum value at point A. The ellipse eccentricity and orientation do not change with time (Fig. 9b).

Variability of the tidal flow in the Fromveur Strait (point B) looks quite different (Fig. 10b). The current velocity rises from 1.7 to 3.8 m/s during the same period whereas the curve of current magnitude variation with time in this point and in the neighboring points is flattened during spring tide, suggesting that the fortnightly modulation of the velocity is affected by non-linear interactions between the tidal constituents. To explore this hypothesis, we performed harmonic analysis of tidal currents in two particular locations: north-west of Ushant Is. (point A), and in the Fromveur strait (point B). The velocity time series were analysed using the Matlab software of Pawlowicz et al. (2002). The results reveal noticeably stronger current magnitude (semi-major axis) of higher order tidal harmonics (M6, 2MS6, 2SM6) (Table 1) indicating their amplification in the strait. This feature also reveals complexity of tidal dynamics in the strait and demonstrates that shallow-water constituents might play an important role in fortnightly modulation through the interaction with principal tidal constituents.

### 3.2. Vorticity field

Surface current vorticity, averaged over the 25-day period in spring, shows patchiness in spatial distribution (Fig. 11a) and some degree of similarity with the spatial pattern of rotary coefficient (Fig. 8b). While in the majority of the domain, vorticity does not exceed  $\pm 2 \cdot 10^{-5} \text{ s}^{-1}$ , much higher values are found around the islands and in the south-eastern sector. These extreme values reach  $-18 \cdot 10^{-5} \text{ s}^{-1}$  for negative, and  $15 \cdot 10^{-5} \text{ s}^{-1}$  for positive vorticity (Fig. 11a) thus evidencing a pronounced rotational character of the surface circulation in the vicinity of islands.

Analysis of instantaneous velocity patterns allows to qualitatively explain the vorticity distribution and to assess its production. The selected spring tide period (18–19 April, 2007) was characterized by moderate northeasterly winds with the relevant circulation patterns shown in Fig. 11b–d. The ebb spring flow is affected by the bottom friction in the vicinity of islands. Thus, southward tidal currents generate a cyclonic eddy on the leeward side of the Ushant Is. (Fig. 11b) and cause positive vorticity production. After the current reversal



**Fig. 9.** (a) Time evolution of the amplitudes of tidal currents in April–May 2007 along the WE-line (Fig. 6c). (b) Evolution of tidal current ellipses at point A (Fig. 6c) located on the WE-line and where the observed surface currents are highest.

(Fig. 11c), the eddy is advected westward by about 10–15 km (location of the second positive vorticity maximum in Fig. 11a), and then disappears during the developing flood. On flood, surface currents skirt around the Ushant and Molène Islands in two branches: stronger western stream, and near-shore eastern stream, also leaking through the Fromveur Strait. Frictional effects generate negative vorticity north of Ushant and Molène Islands and form an eddy (Fig. 11 d). This ccw rotating eddy grows until the current reversal at high water, then disappears during the development of the ebb flow.

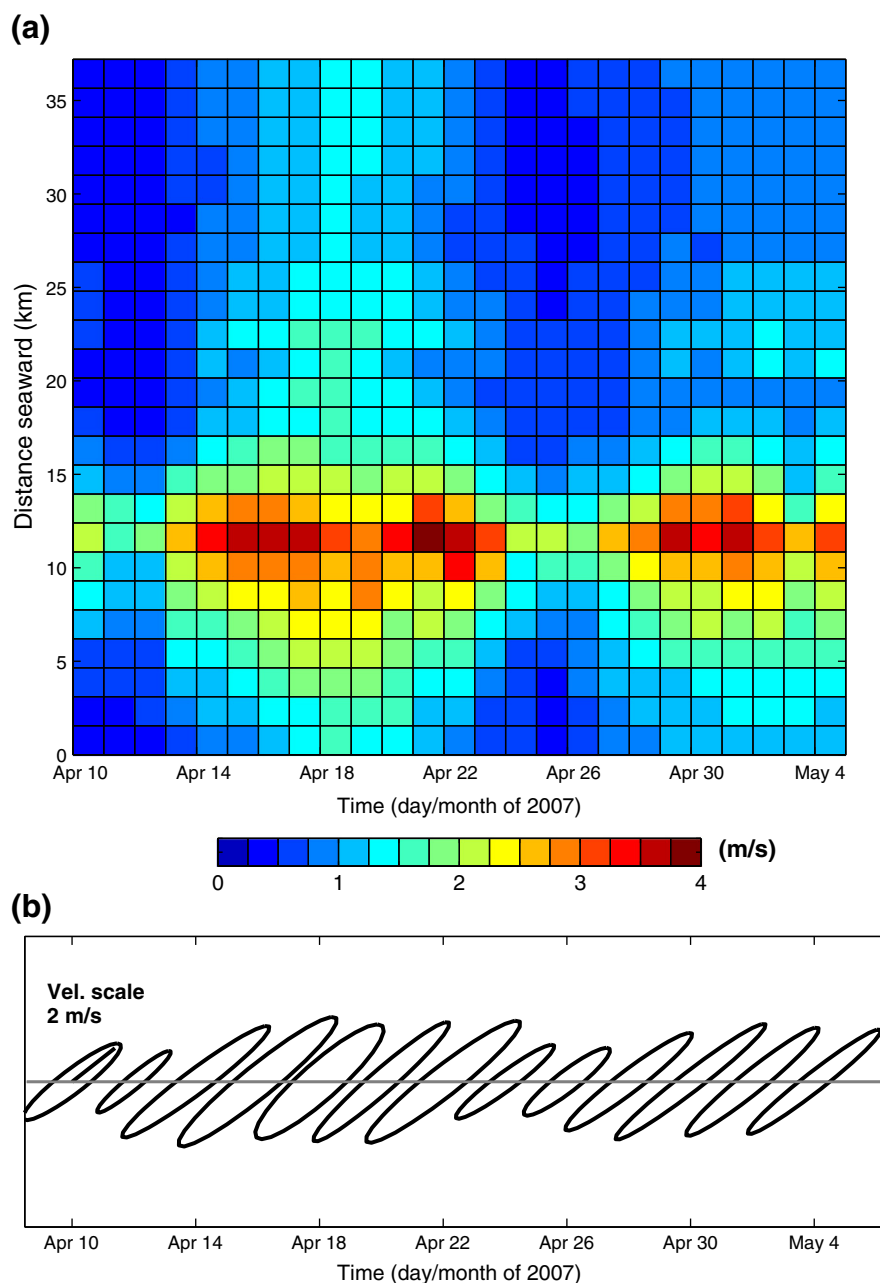
Formation of the cw eddy, partially captured in the south-eastern sector of radar coverage zone (results not shown) follows similar scenario. Negative vorticity is generated by frictional effects of Sein archipelago on the oscillating tidal currents. The maximum values of

vorticity reach  $-12 \cdot 10^{-5} \text{ s}^{-1}$ , indicating generation of an anticyclonic eddy north of the central axis of the archipelago.

Another specific feature of vorticity distribution is a narrow band of negative vorticity surrounding the southwestern and eastern (Fromveur St.) parts of the Ushant Is. (Fig. 11a). This vorticity pattern indicates the dominant cw sign of surface flow around the islands. A transverse circulation induced by a tidal current escalating the depth gradient was analyzed by Godin (1988) who showed that depth gradients and bottom friction tend to veer the mean current to the left of the direction of tidal wave propagation (in the northern hemisphere), align it with the depth contours, thus producing cw rotation of the mean flow.

Spatial distribution of vorticity in summer (results not shown) was found to be very similar to that observed in spring, thus





**Fig. 10.** (a) Time evolution of the amplitudes of tidal currents in April–May 2007 along the FS-line (Fig. 6c). (b) Evolution of tidal current ellipses at point B (Fig. 6c) located in the middle of the Fromveur strait where the observed surface currents are highest.

providing additional support for the permanent character of the observed circulation (vorticity) pattern around islands.

### 3.3. Residual currents

In the tidally dominated basins of the Northwestern European shelf such as the Iroise Sea, Ireland Sea or the English Channel, the

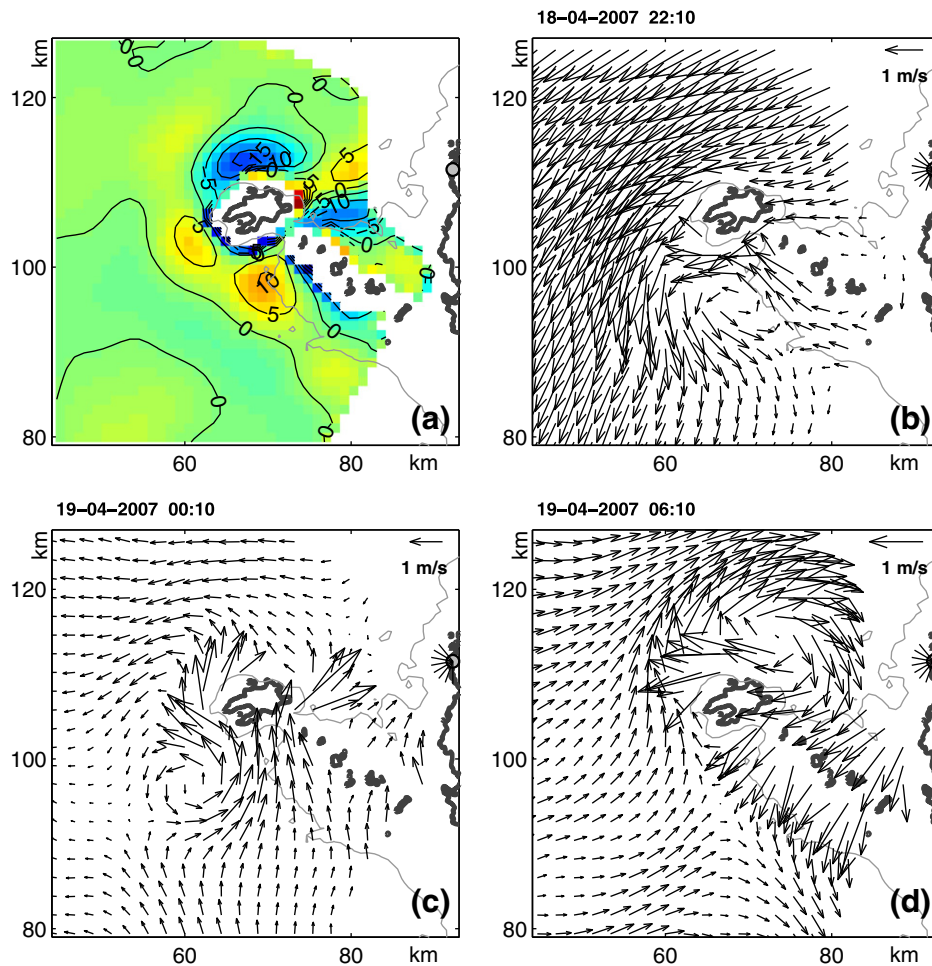
**Table 1**

Semi-major axes (m/s) of tidal current ellipses for the most important tidal constituents in two selected locations: north-west of the Ushant Island (pt. A) and in the Fromveur strait (pt. B in Fig. 6c).

Tidal constit.	M2	S2	N2	M4	MS4	2MN6	M6	2MS6
A: Ushant	1.74	0.92	0.47	0.15	0.16	0.06	0.06	0.08
B: Fromveur	2.09	0.83	0.35	0.12	0.09	0.12	0.16	0.20

long-term averaged currents, referred hereafter as residual currents (RC), might govern the transport of material to a great extent. Therefore, estimation of residual circulation is important for assessing the long-term transport and dispersion of material in tidal flows (Bailly du Bois and Dumas, 2005; Foreman et al., 1992; Zimmerman, 1986). We estimated the residual velocities by averaging the monitored surface currents over each of the two periods under consideration. The resultant fields, shown in Fig. 12a and b, include tidally induced component (major contribution), the wind and buoyancy forced residual flows. The wave induced (Stokes) component was removed beforehand from velocity time series. Fig. 12 clearly demonstrates that control of the residual flow by tidal motions is not prevailing over the area of radar survey, and that tidal and wind forcing might be in competition.

The spatial structure of residual currents for both periods appears complex and allows dividing the basin into two zones: the nearshore



**Fig. 11.** (a) Average vorticity field ( $\times 10^{-5} \text{ s}^{-1}$ ) for April–May period of 2007. (b) Surface currents around Ushant and Molène Islands on ebb during spring tide. Surface currents at the beginning (c) and at the end of flood (d). 50 m isobath is shown by thin grey contour.

zone, with the dominant contribution of tides to RC, and the offshore zone, where wind effect is also playing a significant role. These two zones can be separated by a line slightly west of the 100-m isobath. In the western (offshore) zone, current velocities do not exceed 0.15 m/s in April and 0.25 m/s in September with westward and south-westward directions respectively, indicating the effect of dominant northeasterly and northerly winds during these periods (Fig. 2). On the contrary, in the eastern (nearshore) zone, the RC looks similar for both periods and reveals eddies in the southeastern sector and north of the Ushant Is. There is also a tendency for intensification of the nearshore currents (up to 0.40 m/s) along the 50-m isobath (Fig. 12). The second region of elevated velocities is aligned along the 100-m isobath. Stronger currents (up to 0.40 m/s) occur in the south-eastern part of the domain in the vicinity of Sein archipelago. The velocity drops to 0.20 m/s further northward, and the flow seems to split in two branches. This separation and deflection of currents westward and eastward is probably caused by the bottom irregularity and a promontory visible on the bathymetry map at the intersection of coordinate lines  $x=60$  and  $y=95$  km (Fig. 12a). Currents entering the western offshore zone change direction under the effect of wind forcing, whereas the eastern branch merges with the coastal current. Although the residual current intensification in the Iroise Sea has been already documented (Mariette et al., 1982; Muller et al., 2010), the eddies around the Ushant Is. in the RC field, revealed from the analysis of HFR data set, is a novel feature of tidal dynamics in the area.

The maps of residual velocities for both periods show strong wind forcing control in the western zone and topographic control in the

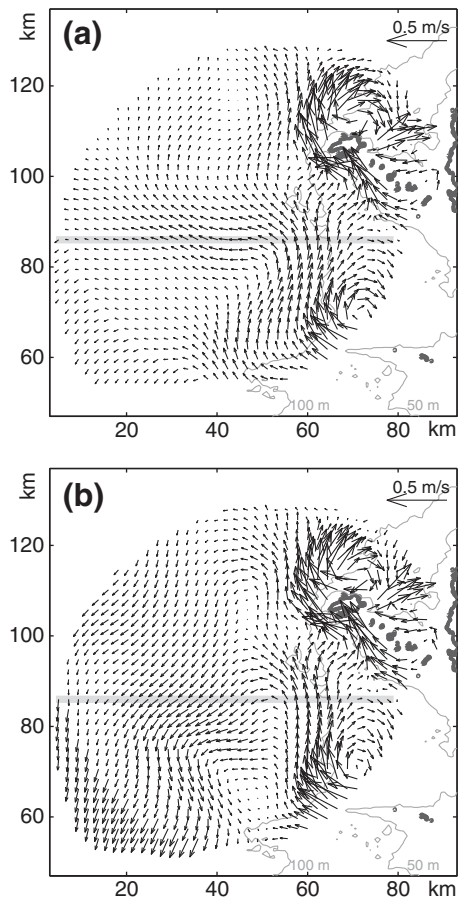
eastern zone. The response of surface currents to wind forcing was further examined statistically by assuming the following relation for the (non-tidal) residual times series (Prandle and Matthews, 1990):

$$R(t) = \bar{R} + \alpha \tau(t - \Delta t), \quad (1)$$

where  $\bar{R}$  is the steady non-wind-driven residual current,  $\Delta t$  is a time lag between wind and surface current response, and  $\alpha$  is a complex-valued coefficient. Both  $\bar{R}$  and  $\alpha$  vary in space.  $\tau$  is the wind stress calculated from the hourly wind data of met buoy and assumed to be power-law function of the wind speed  $W^n$ . The complex current vector  $R(t)$  was derived from low-pass filtered HFR surface current velocities. The filter reduces tidal (diurnal, semidiurnal) and inertial variability to less than 1% of their original values, and passes 90% or more of the low-frequency signal (Stacey et al., 1986). The wind hourly data were smoothed by 24-h moving average. The values of  $\bar{R}$  and  $\alpha$  were calculated by least-squares fitting for different powers of the wind speed,  $W$ , and time lag  $\Delta t$ . The overall correlations between the observed and estimated residual velocities were weakly sensitive to the parameter  $n$  of the wind speed, but showed significant dependence on the time lag (in the range 0–12 h). The maximum correlation, 0.86, was found for a time lag of 4 h and  $\tau \propto W^2$ . The optimal values of  $\alpha$  (providing maximum correlation) were then used in combination with the wind stress to subtract the wind response from surface velocity time series.

Two situations were explored. In the first situation, only tidal motions were removed from velocity time series  $R(t)$ . Then, the wave induced surface currents, retrieved by the method described in





**Fig. 12.** Eulerian residual surface currents during the 26-day period in April–May 2007 (a) and late summer period, August–September 2007, (b). Grey lines indicate the location of east–west cross section used for assessment of residual current variability. 50 m and 100 m isobaths are shown by thin grey contours.

Section 2.2.5, were also subtracted from these time series, and the least-squares fit of surface velocities to wind forcing was performed. The results revealed high sensitivity of surface residuals to wave-induced forcing, which in turn contains the wind effect. The contribution of wave induced currents to surface residuals was found particularly important in the eastern shallow water part of the domain during the late summer period (when winds were blowing from the northern sector). The values of wave-induced velocity in the vicinity of Ushant and Molène Islands attain 0.15–0.18 m/s (cf. Section 2.2.5) and become comparable with the magnitude of the residual currents in this area.

In Fig. 13a, we show the northern component of de-tided velocity time series for April, and in Fig. 13b, velocities from which the major contribution of wind and waves were removed by linear regression method. We examine the time variability of this velocity component across a horizontal line located approximately in the middle of the HFR coverage zone (Fig. 12). Fig. 13a reveals existence of a permanent northward residual current, following the 100-m isobath. The velocity magnitude varies in time from 0.05 to 0.20 m/s indicating a low-frequency modulation of the RC by atmospheric forcing. Northern and north-eastern winds observed during the first 4-day period (Fig. 2b) significantly weaken the current to 0.01 m/s. In the eastern nearshore part of the section, southward residual currents persist during the whole period of analysis, with velocities up to 0.10 m/s (Fig. 13a). In the western (offshore) sector, the current changes the sign to positive with each reversal of the wind direction.

The removal of wind-wave effect allows better understanding of RC variability (Fig. 13b). The major apparent difference, compared

to Fig. 13a, is the dominant northward flow over the majority of the cross-section, with the exception of the eastern limit influenced by the anti-cyclonic eddy (cf. Fig. 12a). The change in sign of the current direction, observed on April 14–17 and 22–26, indicates a low frequency variability of the RC, caused by a mechanism different from wave and wind forcing. This variability also results in a periodic increase of current velocity up to 0.22 m/s within the near-shore jet.

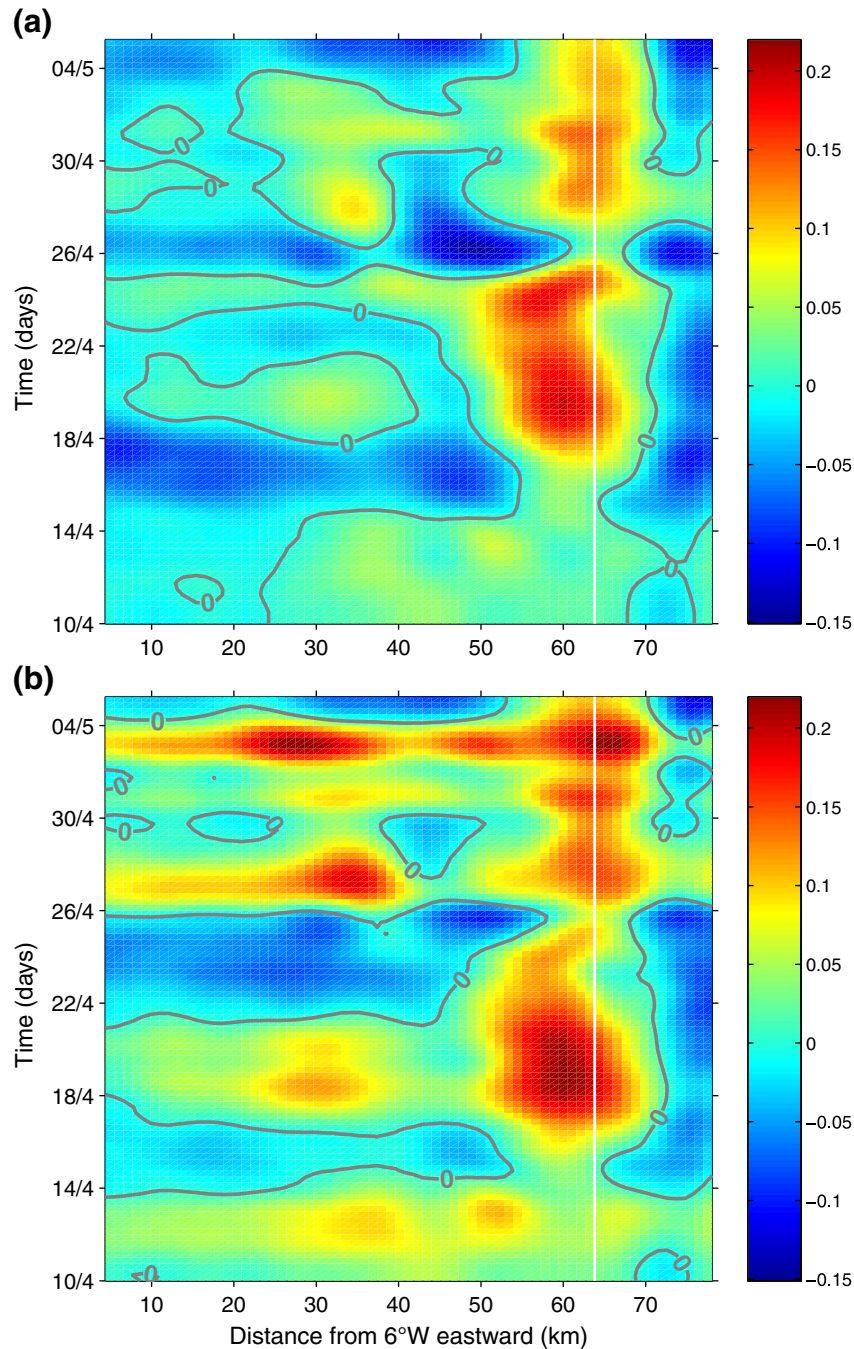
During the late summer period, the RC looks quite different (Fig. 14): the northward current (approximately following the 100-m isobath) keeps its spatial shape and high magnitude in the eastern part of the section, the dominant flow appears clearly southward in the western part of the section. Removal of the wind- and wave-induced currents modifies the circulation pattern (Fig. 14b) and suggests that other forcing (e.g. baroclinic) might come into play and contribute to the RC formation in the region. Positive velocities of the RC, observed close to the western limit of the domain between 11 and 18 September (Fig. 14b), support this hypothesis: field studies performed in this area during the same period (Le Boyer et al., 2009), indicated meandering of the bottom thermal front which might contribute to generation of a filament with positive (northward) velocities separating from the main northward branch of the RC (Fig. 14b). It should also be noted that a signature of the wind forcing still remains non-negligible in the RC during the period of strong northern winds. Detailed investigation of the circulation in the period of Ushant thermal front development is a subject of our future work.

#### 4. Discussion and conclusions

The experiment reported in this paper is based on the employment of a HFR system to study circulation in highly energetic tidal basin – the Iroise Sea. The radar-derived surface currents were investigated for two selected periods by means of various numerical and statistical techniques. We managed to obtain surface currents at higher resolution, due to application of the MUSIC (direction finding) technique in conjunction with variational 2dVar interpolation. This approach provided significant level of confidence in the surface flow retrieved from HFR data. Estimated accuracy of the surface velocities was found to be less than 0.15 m/s (30%) in the majority of the radar coverage zone (Fig. 6), whereas the mean velocity, averaged in space and time for the first period of observations, is close to 0.50 m/s.

The radar derived velocity data reveal flow complexity and variability at a level of details that were not previously available. Though there have been a number of important field investigations (Ardhuin et al., 2009; Le Boyer et al., 2009) and numerical studies of circulation in the Iroise Sea (Muller et al., 2009, 2010), the presented radar survey have brought a significant contribution to understating physical processes governing the coastal water dynamics in the region where the tidal currents attain one of the highest values on the North-European shelf. Previous reconstructions of the surface currents in the Iroise Sea have never documented velocities close to 4 m/s, neither provided detailed spatial patterns of velocity fields. The angular resolution of the BF method, routinely used in processing the HFR data, is too coarse and, in our opinion, unable to capture the fine scale structure of the surface flow, especially around islands and in the Fromveur Strait which are of particular interest. An effort to employ the OMA technique (Kaplan and Lekien, 2007) for interpolating radial velocities provides much less details (cf. Fig. 8, Muller et al., 2009) due to intrinsic limitations of the method and coarse resolution of radial velocity fields.

Our analyses have shown that surface circulation in the Iroise Sea is dominated by tides and winds. The wave induced component of surface currents is less important, while the buoyancy forcing (due to freshwater input) was negligible during the study period. Complex bottom topography, numerous islets and rocks, partially exposed at low water, make the local circulation noticeably different from that observed by oceanographic coastal radars in other regions of the



**Fig. 13.** (a) South–north component of de-tided surface residuals along the W–E line (shown by grey shading in Fig. 12), and long-term time-dependent surface residuals (South–north component) along the W–E line (b) for April–May period 2007. White vertical line indicates the location of 100 m isobath on the section.

North-European tidal seas (Carbajal and Pohlmann, 2004; De Valk, 1999; Matthews et al., 1993; Sentchev and Yaremchuk, 2007). The major differences are the extremely large magnitude of tidal currents, their high spatial variability inducing a pronounced eddy character of near-shore circulation resulting in a complex permanent structure of the residual velocity field.

Refined resolution allowed us to detect and obtain *quantitative estimates* of the following circulation features:

1. A prominent dipole structure in the vorticity field characterized by two oppositely rotating eddies, with the maximum vorticity of  $-1.8 \cdot 10^{-4} \text{ s}^{-1}$  and  $1.5 \cdot 10^{-4} \text{ s}^{-1}$  for the northern and southern eddies, generated on the leeward side of the Ushant Is. on flood

and ebb respectively. Mechanisms of vorticity production were described in detail by Pingree and Maddock (1985); Orbi and Salomon (1988). Vorticity of the opposite sign is locally generated by both bottom friction effects and velocity gradients with respect to the direction of tidal flow. Advection by current of the negative vorticity during flood, and positive vorticity during ebb, results in appearance of two distinct zones of opposite vorticity (dipole type structure) on each side of the island: negative vorticity north of the Ushant Island and positive vorticity south of the island. Our experimental results are in close agreement with these theoretical considerations. Analysis of the average divergence field (results not shown) revealed several characteristic structures which seem to be related to tidal generated eddies. In particular, a

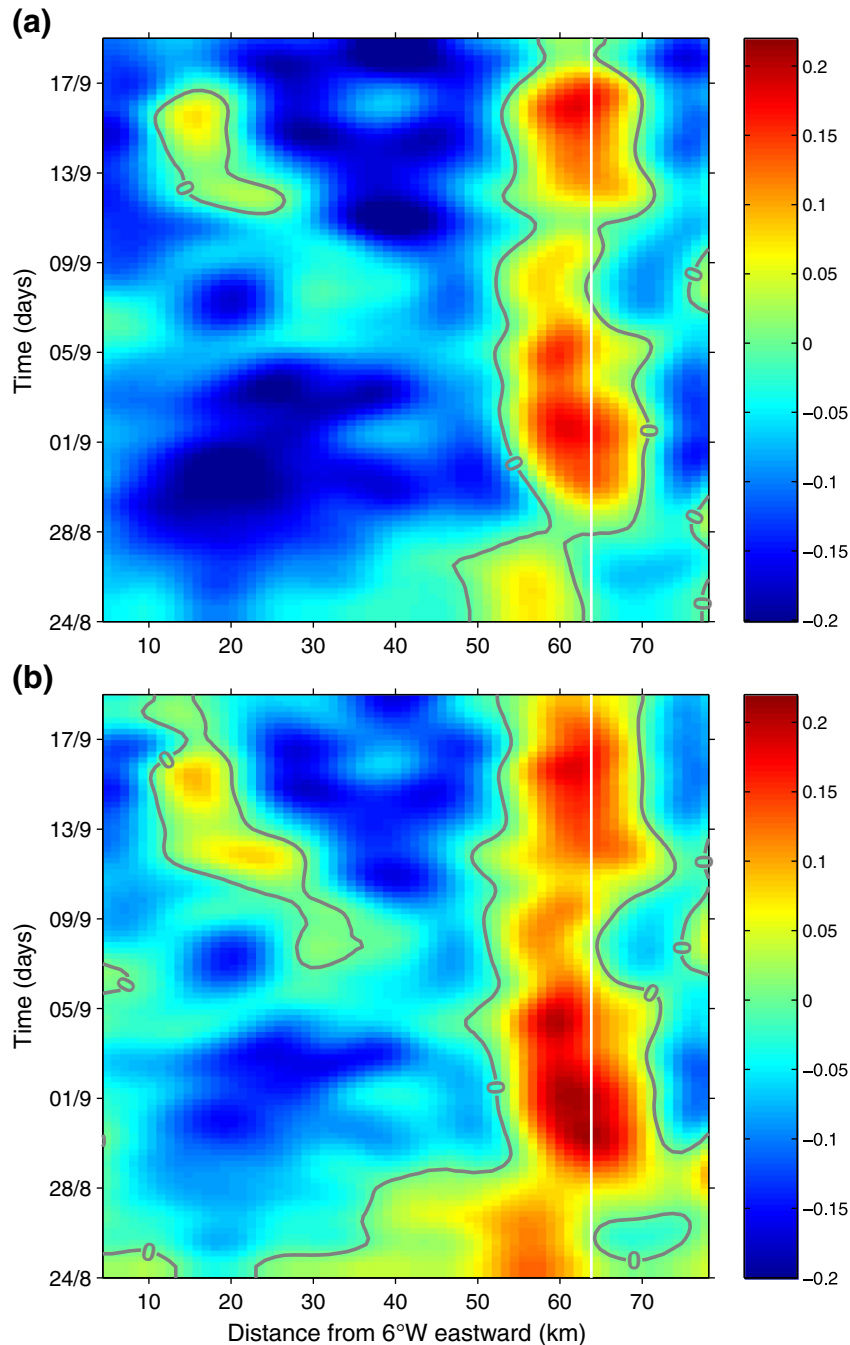


Fig. 14. Same as Fig. 11 but for August–September 2007.

bi-pole structure of divergence with different polarity occurs west of Ushant Island, and is obviously related to eddies generated by oscillating tidal currents.

2. Spatial intermittence in polarization of ellipses has been diagnosed. Positive (ccw) rotation of the tidal currents with amplitudes up to 1.5 m/s in the shallow water region between the Brittany coast and Molène Islands has been detected. This feature is likely to be generated by the bottom friction effect, particularly important at ebb, when a large area between the Molène Islands and the Brittany coast becomes free of water. This is known as “beach drying” phenomenon (Prandle, 1982). Positive polarization south of the Ushant Is. is related to positive vorticity ( $0.5\text{--}1.5 \cdot 10^{-4} \text{ s}^{-1}$ ) of currents in this area.
3. The spatial pattern of the residual currents can be characterized by two distinct zones approximately separated by the 100 m isobath:

In the western (offshore) zone, residual currents have a significant contribution of the wind-driven component, whereas the near-shore zone is characterized by extremely strong (up to 0.4 m/s) tidally generated residual circulation.

4. Residual currents in the nearshore (eastern) zone form two anticyclonic eddies: north of the western extremity of the Sein archipelago, and north the Ushant Is. The maximum velocity in these eddies reaches 0.4 m/s. The mean velocity field inferred from the HFR data, contains a signature of two along-shore jets approximately following the 100 m (minor jet) and 50 m depth contours (major jet) and merging south of the Ushant Is. in a 0.5 m/s strong flow. Qualitatively, our results are consistent with estimates of the Eulerian residual velocities from the numerical experiments of Muller et al. (2009) and from the analysis of currents from ARGOS drifters (Muller et al., 2010).



5. An extremely strong (four-fold) fortnightly modulation of tidal currents is documented northwest of the Ushant Is. The interference of the major semi-diurnal tidal constituents ( $M_2$ ,  $S_2$  and  $N_2$ ) provides the major part of the variability of currents there. We also diagnosed a significant contribution of the higher order non-linear tidal harmonics ( $M_6$ ,  $2MS_6$ ,  $2SM_6$ ) to the surface current in the Fromveur strait. Here, the sixth-diurnal and quarter-diurnal tidal harmonics are comparable in strength (Table 1), and their interference affects the shape of fortnightly modulation of the current by flattening its maxima and amplifying its minima.

A long-term, time-dependent, component of residual currents has been estimated and assessed. Specific features of this component are: separation of the basin in two zones, offshore and nearshore, with different control of the RC and low-frequency (weekly) modulation of the flow in April–May, 2007. The comparison of the RC fields for spring and late summer periods revealed substantial difference in the offshore and similarity in the near-shore circulation patterns suggesting a quasi-permanent character of the residual flow of the latter.

Our analysis have also shown that the magnitude of variation of the offshore flow and the mean velocity of permanent (nearshore) flow are comparable. Therefore, periodic tidal forcing superimposed on the residual velocity shear may result in strong variations of the tracer trajectories released at different phases of the tidal cycle (Foreman et al., 1992; Zimmerman, 1986), and cause strong dispersion of the material.

The acquired data and the presented results could be very useful for coastal circulation model validation and initialization, comprehension and interpretation of remote sensing images (Le Boyer et al., 2009), and also for studying specific issues such as eddy, thermal tidal front dynamics, high resolution Lagrangian circulation and passive tracer dynamics in this region.

## Acknowledgments

The study was performed in the framework of Epigram (Etudes Physiques Intégrées en Gascogne et Région Atlantique-Manche) scientific project (Yves Morel (LEGOS), head of the project) funded by the ANR (Agence Nationale de la Recherche) and INSU (Institut National des Sciences de l'Univers). The HFR data were provided by ACTIMAR with the authorisation of the French Naval Oceanographic Centre (SHOM). Meteorological data have been provided by regional office of Météo-France. Part of the work was completed when one of the authors (MY) was visiting the Université du Littoral with support from the French Ministry of Education and Research. We would like also to thank Louis Marié and Fabrice Ardhuin for help with the data.

## Appendix. Wave-driven contribution to radar derived surface current

The surface current measured by radar writes:

$$\mathbf{U} = \mathbf{U}_E + \mathbf{U}_{SS}, \quad (\text{A1})$$

where,  $\mathbf{U}_E$  is the quasi-Eulerian surface current, i.e. the current at a depth of  $\approx \lambda/8\pi$  with  $\lambda$  the radar wavelength (Stewart and Joy, 1974), and  $\mathbf{U}_{SS}$  represents the specific contribution of the sea state. Let us define a function  $\mathbf{u}(f)$  as:

$$\mathbf{u}(f) = 4\pi \int_0^f \int_0^{2\pi} \mathbf{k} E(f, \theta) df d\theta, \quad (\text{A2})$$

with  $f$  the wave frequency,  $\mathbf{k}$  the wavenumber and  $E(f, \theta)$  the sea surface elevation spectrum.  $\mathbf{U}_{SS}$  writes as (Broche et al., 1983):

$$\mathbf{U}_{SS} = \mathbf{u}(f_B) + \mathbf{M}, \quad (\text{A3})$$

where  $f_B$  is the Bragg frequency (0.359 Hz for a radar frequency of 12.4 MHz). Computations show that  $\mathbf{M}$ , which is not developed

here, is a small term compared to  $\mathbf{u}$  at present radar frequency. Then  $\mathbf{U}_{SS}$  is nearly equal to the contribution of the total surface Stokes drift,  $\mathbf{u}(\infty)$ , of the waves with frequencies below  $f_B$ .

As an output, the wave model WW3 provides an approximation to  $\mathbf{u}(\infty)$ , namely  $\mathbf{u}(f_c)$ , where  $f_c = 0.72$  Hz is the cutoff frequency of the model. Recently, Ardhuin et al. (2009) proposed a robust approximation for  $\mathbf{u}(f)$  (the norm of  $\mathbf{u}(f)$ ) in terms of the local 10-meter wind speed  $U_{10}$  and the significant wave height  $H_s$

$$\mathbf{u}(f) = 5 \cdot 10^{-4} \left( 1.25 - 0.25(0.5/f)^{1.3} \right) U_{10} \min(U_{10}, 14.5) + 0.025(H_s - 0.4) \quad (\text{A4})$$

Eliminating  $U_{10}$  between the two equations formed by Eq. (4) with  $f = f_B$  and  $f = f_c$  respectively, and neglecting  $\mathbf{M}$ , one can obtain

$$U_{SS} = 0.79u(f_c) + 5.2510^{-3}(H_s - 0.4). \quad (\text{A5})$$

The analysis of the model data for the experimental period has shown that (A5) can be further simplified to  $U_{SS} = 0.85u(f_c)$ .

We take as direction of  $\mathbf{U}_{SS}$  the direction of  $\mathbf{u}(f_c)$ .

## References

- Ardhuin, F., Marié, L., Rasche, N., Forget, P., Roland, A., 2009. Observation and estimation of Lagrangian, Stokes and Eulerian currents induced by wind and waves at the sea surface. *J. Phys. Oceanogr.* 39, 2820–2838.
- Bailly du Bois, P., Dumas, F., 2005. Fast hydrodynamic model for medium- and long-term dispersion in seawater in the English Channel and southern North Sea, qualitative and quantitative validation by radionuclide tracers. *Ocean Model.* 9, 169–210.
- Barrick, D.E., Lipa, B.J., 1996. A comparison of direction-finding and beam-forming in HF radar ocean surface current mapping. Phase I SBIR Final Rep., Contract 50-DKNA-5-00092. . 80 pp.
- Barrick, D.E., Lipa, B.J., 1997. Evolution of bearing determination in HF current mapping radars. *Oceanography* 10 (2), 72–75.
- Bassin, C.J., Wa'zshburn, L., Brzezinski, M., McPhee-Shaw, E., 2005. Sub-mesoscale coastal eddies observed by high frequency radar: a new mechanism for delivering nutrients to kelp forests in the Southern California Bight. *Geophys. Res. Lett.* 32.
- Bouligand, R., Pirazzoli, P.A., 1999. Les surcotes et les décotes marines à Brest, étude statistique et évolution. *Oceanol. Acta* 22–2, 153–166.
- Breivik, O., Sætra, O., 2001. Real time assimilation of HF radar currents into a coastal ocean model. *J. Mar. Syst.* 28, 161–182.
- Broche, P., De Maistre, J.C., Forget, P., 1983. Mesure par radar décimétrique cohérent des courants superficiels engendrés par le vent. *Oceanol. Acta* 6, 43–53.
- Carbajal, N., Pohlmann, T., 2004. Comparison between measured and calculated tidal ellipses in the German Bight. *Ocean Dyn.* 54, 520–530.
- De Valk, C.F., 1999. Estimation of 3-D current fields near the Rhine outflow from HF radar surface current data. *Coast. Eng.* 37, 487–511.
- Defant, A., 1961. *Physical Oceanography*. Pergamon, NY. 725 pp.
- Emery, W.J., Thompson, R.E., 1997. *Data Analysis Methods in Physical Oceanography*. Pergamon, NY. 634 pp.
- Foreman, M.G.G., Baptista, A.M., Walters, R.A., 1992. Tidal model studies of particle trajectories around a shallow coastal bank. *Atmosphere-Ocean* 30, 43–49.
- Godin, G., 1988. Tides. CICESE, Ensenada B.C, Mexico.
- Gurgel, K.W., Barbin, Y., 2008. Suppressing radio frequency interference in HF radars. *Sea Technology* 49, 39–42.
- Haus, B.K., Wang, J.D., Rivera, J., Smith, N., Martinez-Pedraja, J., 2000. Remote radar measurement of shelf currents off Key Largo, Florida. *Estuarine Coastal Shelf Sci.* 51, 553–569.
- Kaplan, D., Lekien, F., 2007. Spatial interpolation and filtering of surface current data based on open-boundary modal analysis. *J. Geophys. Res.* 112, C10027. doi:10.1029/2006JC003984.
- Kaplan, D.M., Largier, J.L., Botsford, L.W., 2005. HF radar observations of surface circulation off Bodega Bay (northern California, USA). *J. Geophys. Res.* 110, C10020. doi:10.1029/2005JC002959.
- Kovacevic, V., Gacic, M., Mancero, Mosquera I., Mazzoldi, A., Marinetti, S., 2004. HF radar observations in the northern Adriatic: surface current field in front of the Venetian Lagoon surf. *J. Mar. Syst.* 51, 95–122.
- Le Boyer, A., Cambon, G., Daniault, N., Herbet, S., Le Cann, B., Marié, L., Morin, P., 2009. Observations of the Ushant tidal front in September 2007. *Cont. Shelf Res.* 29, 1026–1037.
- Lipa, B., Nyden, B., Ullman, D.S., Terrill, E., 2006. SeaSonde radial velocities: derivation and internal consistency. *IEEE J. Oceanic Eng.* 31 (4), 850–861.
- Lux, M., Penard, C., Cancet, M., Lyard, F., Lamouroux, J., Bourgogne, S., Bronner, E., 2010. COMAPI: New regional tide solutions and high frequency dynamical atmospheric corrections. OST-ST Meeting 2010, Altimetry for Oceans and Hydrology, 18–22 October, Lisbon, Portugal.
- Mariette, V., Le Cann, B., 1985. Simulation of the formation of the Ushant thermal front. *Cont. Shelf Res.* 4, 637–660.

- Mariette, V., Rougier, G., Salomon, J.C., Simon, B., 1982. Courants de marée en Mer d'Iroise. *Oceanol. Acta* 5, 149–159.
- Mariette, V., Thomas, N., Cochin, V., Guichoux, Y., Arduin, F., 2006. Premiers résultats de l'expérience SURLITOP (Surveillance Littorale Opérationnelle). *Navigation* 54, 45–57.
- Marmorino, G.O., Shay, L.K., Haus, B.K., Handler, R.A., Graber, H.C., Horne, M.P., 1999. An EOF analysis of HF Doppler radar current measurements of the Chesapeake Bay buoyant outflow. *Cont. Shelf Res.* 19, 271–288.
- Matthews, J., Fox, A., Prandle, D., 1993. Radar observation of an along-front jet and transverse flow convergence associated with a North Sea front. *Cont. Shelf Res.* 13, 109–130.
- Muller, H., Dumas, F., Blanke, B., Mariette, V., 2007. High resolution atmospheric forcing for regional oceanic model: the Iroise Sea. *Ocean Dyn.* 57, 375–400. doi:[10.1007/s10236-007-0115-4](https://doi.org/10.1007/s10236-007-0115-4).
- Muller, H., Dumas, F., Blanke, B., Mariette, V., 2009. Estimating the Lagrangian residual circulation in the Iroise Sea. *J. Mar. Syst.* 78 (Suppl. 1), S17–S36. doi:[10.1016/j.jmarsys.2009.01.008](https://doi.org/10.1016/j.jmarsys.2009.01.008).
- Muller, H., Blanke, B., Dumas, F., Mariette, V., 2010. Identification of typical scenarios for the surface Lagrangian residual circulation in the Iroise Sea. *J. Geophys. Res.* 115, C07008. doi:[10.1029/2009JC005834](https://doi.org/10.1029/2009JC005834).
- Orbi, A., Salomon, J.C., 1988. Tidal dynamics in the vicinity of the Channel Islands. *Oceanol. Acta* 11, 55–64.
- Pawlowicz, R., Beardsley, R., Lentz, S., 2002. Classical tidal harmonic analysis including error estimates in MATLAB using T\_Tide. *Comput. Geosci.* 28, 929–937.
- Pingree, R.D., Maddock, L., 1985. Rotary currents and residual circulation around banks and islands. *Deep-Sea Res.* 32, 929–947.
- Pingree, R.D., Pugh, P.R., Holligan, M., Forster, G.R., 1975. Summer phytoplankton blooms and red tides along tidal fronts in the approaches to the English Channel. *Nature* 258, 672–677. doi:[10.1038/258672a0](https://doi.org/10.1038/258672a0).
- Prandle, D., 1982. The vertical structure of tidal currents and other oscillatory flows. *Cont. Shelf Res.* 1, 191–207.
- Prandle, D., Matthews, J., 1990. The dynamics of nearshore surface currents generated by tides, wind and horizontal density gradients. *Cont. Shelf Res.* 10, 665–681.
- Schmidt, R.O., 1986. Multiple emitter location and signal parameter estimation. *IEEE Trans. Antennas Propag.* AP-34, 276–280.
- Sentchev, A., Yaremchuk, M., 2007. VHF radar observations of surface currents off the northern Opal coast in the eastern English Channel. *Cont. Shelf Res.* 27, 2449–2464.
- Sentchev, A., Forget, P., Barbin, Y., 2009a. Residual and tidal circulation revealed by VHF radar surface current measurements in the southern Channel Isles region (English Channel). *Estuarine Coastal Shelf Sci.* 82, 180–192. doi:[10.1016/j.ecss.2008.12.003](https://doi.org/10.1016/j.ecss.2008.12.003).
- Sentchev, A., Forget, P., Yaremchuk, M., Barbin, Y., 2009b. Application of Variational Interpolation for Fitting Sparsely Sampled Radar Velocity Data in The Gulf of Lions. 9th International Radiowave Oceanography Workshop (ROW-9), 18–22 May 2009, Split, Croatia.
- Stacey, M.W., Pond, S., LeBlond, P.H., 1987. An analysis of the low-frequency current fluctuations in the Strait of Georgia, from June 1984 until January 1985. *J. Phys. Oceanogr.* 17, 326–342.
- Stewart, R.H., Joy, J.W., 1974. HF radio measurements of surface currents. *Deep-Sea Res.* 21, 1039–1049.
- Weber, B.L., Barrick, D.E., 1977. On the nonlinear theory for gravity waves on the ocean's surface Part 1: derivations. *J. Phys. Oceanogr.* 7, 3–10.
- Yaremchuk, M., Sentchev, A., 2009. Mapping radar-derived sea surface currents with a variational method. *Cont. Shelf Res.* 29, 1711–1722.
- Yoshikawa, Y., Matsuno, T., Marubayashi, K., Fukudome, K., 2007. A surface velocity spiral observed with ADCP and HF radar in the Tsushima Strait. *J. Geophys. Res.* 112, C06022. doi:[10.1029/2006JC003625](https://doi.org/10.1029/2006JC003625).
- Zimmerman, J.T.F., 1986. The tidal whirlpool: a review of horizontal dispersion by tidal and residual currents. *Neth. J. Sea Res.* 20, 133–154.